

Journal of Geophysical Research: Space Physics

RESEARCH ARTICLE

10.1002/2014JA019930

This article is a companion to Wilson et al. [2014], doi:10.1002/2014JA019929.

Key Points:

- Microscopic wave-particle interactions can regulate macroscopic shock structure
- High-frequency large-amplitude waves are ubiquitous in collisionless shocks
- Wave-particle interactions are the end result of nearly all dissipation pathways

Correspondence to:

L. B. Wilson III,
 lynn.b.wilsoniii@gmail.com

Citation:

Wilson, L. B., III, D. G. Sibeck, A. W. Breneman, O. Le Contel, C. Cully, D. L. Turner, V. Angelopoulos, and D. M. Malaspina (2014), Quantified energy dissipation rates in the terrestrial bow shock: 2. Waves and dissipation, *J. Geophys. Res. Space Physics*, 119, 6475–6495, doi:10.1002/2014JA019930.

Received 4 MAR 2014

Accepted 23 JUL 2014

Accepted article online 29 JUL 2014

Published online 25 AUG 2014

Quantified energy dissipation rates in the terrestrial bow shock: 2. Waves and dissipation

L. B. Wilson III¹, D. G. Sibeck¹, A. W. Breneman², O. Le Contel³, C. Cully⁴, D. L. Turner⁵, V. Angelopoulos⁵, and D. M. Malaspina⁶

¹NASA Goddard Space Flight Center, Greenbelt, Maryland, USA, ²School of Physics and Astronomy, University of Minnesota, Minneapolis, Minnesota, USA, ³Laboratoire de Physique des Plasmas, Ecole Polytechnique, Palaiseau, France, ⁴Department of Physics and Astronomy, University of Calgary, Calgary, Alberta, Canada, ⁵Institute of Geophysics and Planetary Physics/Earth and Space Sciences, University of California, Los Angeles, California, USA, ⁶Laboratory for Atmospheric and Space Physics, University of Colorado Boulder, Boulder, Colorado, USA

Abstract We present the first quantified measure of the energy dissipation rates, due to wave-particle interactions, in the transition region of the Earth's collisionless bow shock using data from the Time History of Events and Macroscale Interactions during Substorms spacecraft. Our results show that wave-particle interactions can regulate the global structure and dominate the energy dissipation of collisionless shocks. In every bow shock crossing examined, we observed both low-frequency (<10 Hz) and high-frequency (≥ 10 Hz) electromagnetic waves throughout the entire transition region and into the magnetosheath. The low-frequency waves were consistent with magnetosonic-whistler waves. The high-frequency waves were combinations of ion-acoustic waves, electron cyclotron drift instability driven waves, electrostatic solitary waves, and whistler mode waves. The high-frequency waves had the following: (1) peak amplitudes exceeding $\delta B \sim 10$ nT and $\delta E \sim 300$ mV/m, though more typical values were $\delta B \sim 0.1$ –1.0 nT and $\delta E \sim 10$ –50 mV/m; (2) Poynting fluxes in excess of $2000 \mu\text{W m}^{-2}$ (typical values were ~ 1 –10 $\mu\text{W m}^{-2}$); (3) resistivities $> 9000 \Omega \text{ m}$; and (4) associated energy dissipation rates $> 10 \mu\text{W m}^{-3}$. The dissipation rates due to wave-particle interactions exceeded rates necessary to explain the increase in entropy across the shock ramps for $\sim 90\%$ of the wave burst durations. For $\sim 22\%$ of these times, the wave-particle interactions needed to only be $\leq 0.1\%$ efficient to balance the nonlinear wave steepening that produced the shock waves. These results show that wave-particle interactions have the capacity to regulate the global structure and dominate the energy dissipation of collisionless shocks.

0.1–1nT
 10–50mV/m

1. Introduction

Understanding energy dissipation mechanisms in collisionless shock waves has been a topic of great interest since their prediction over 50 years ago [Petschek, 1958]. Collisionless media (e.g., terrestrial bow shock) cannot rely upon binary particle collisions to irreversibly transform the bulk flow kinetic energy into heat. Therefore, they require other mechanisms including: dispersive radiation [e.g., Tidman and Northrop, 1968], macroscopic quasi-static field effects [e.g., Hull and Scudder, 2000], particle reflection [e.g., Edmiston and Kennel, 1984], and wave-particle interactions [e.g., Sagdeev, 1966]. Theory [e.g., Sagdeev, 1966; Coroniti, 1970] predicts that the dominant mechanism depends upon macroscopic parameters, such as the fast mode Mach number, M_f , the angle, θ_{bn} , between the average upstream magnetic field and the shock normal vector, \hat{n} , and the ratio of particle to magnetic pressures called the plasma beta, β . For instance, low M_f quasi-perpendicular (i.e., $\theta_{\text{bn}} \geq 45^\circ$) shocks are predicted to depend upon dispersive radiation and/or wave-particle interactions [Kennel et al., 1985]. At higher M_f , macroscopic quasi-static fields and particle reflection start to become more important through multistep processes that ultimately end with microscopic wave-particle interactions [e.g., Tidman and Krall, 1971; Wu et al., 1984; Treumann, 2009]. Though generalized predictions have been theorized, the relative importance of each energy dissipation mechanism is not quantifiably understood for low-to-mid Mach number shocks.

It is well known that the macroscopic magnetic field profile of a shock can change dramatically between quasi-perpendicular ($\theta_{\text{bn}} > 45^\circ$) and quasi-parallel ($\theta_{\text{bn}} \leq 45^\circ$) geometry, due to the foreshock and its associated fluctuations [e.g., Greenstadt et al., 1975, 1977; Kennel et al., 1985; Schwartz and Burgess, 1991]. The macroscopic magnetic field profile is theoretically dependent upon M_f as well, but recent observations [e.g., Wilson et al., 2012] have shown that previous observations [e.g., Farris et al., 1993] of laminar shock

Different mechanisms for low and high Mach number shocks.

Observations of laminar shocks
may have been under-sampled!

magnetic field profiles may have been under-sampled. While previous studies of high-frequency waves in collisionless shocks found an amplitude dependence on M_f [e.g., Wilson *et al.*, 2007], the occurrence of the high-frequency waves of interest in this study did not depend upon θ_{Bn} . In addition, the Mach numbers examined herein (~ 2 – 6) are consistent with those in the work by Wilson *et al.* [2007]. Thus, we will not focus on dependencies on M_f or θ_{Bn} herein.

As we discussed in the companion paper [Wilson *et al.*, 2014] (from herein called Paper I), the first three methods have multiple pathways to dissipate energy but nearly all end with microscopic processes involving wave-particle interactions. In addition, previous studies of collisionless shocks have found any combination of the following electromagnetic and electrostatic fluctuations: (1) magnetosonic whistler waves [e.g., Hull *et al.*, 2012; Sundkvist *et al.*, 2012; Wilson *et al.*, 2009, 2012], (2) high-frequency electromagnetic whistler mode waves [e.g., Hull *et al.*, 2012; Wilson *et al.*, 2013a], (3) trains of electrostatic solitary waves (ESWs) or electron phase space holes [e.g., Bale *et al.*, 1998, 2002; Wilson *et al.*, 2010], (4) ion-acoustic waves (IAWs) [e.g., Fuselier and Gurnett, 1984; Balikhin *et al.*, 2005; Wilson *et al.*, 2007], and/or (5) the electron cyclotron drift instability (ECDI) [Breneman *et al.*, 2013; Wilson *et al.*, 2010]. Note that the ECDI is an instability, not a wave. It radiates electron Bernstein modes and ion-acoustic modes, which couple and are observed as a broad acoustic spectrum with superposed cyclotron harmonics (see section 4.2 and Appendix A for more details). For brevity, we will use ECDI when referring to the mixture of these modes herein.

Previous studies focusing on electric field observations of some of the higher-frequency modes observed amplitudes exceeding ~ 200 mV/m [e.g., Breneman *et al.*, 2013; Hull *et al.*, 2006; Mozer and Sundkvist, 2013; Wilson *et al.*, 2007, 2010]. Recent Vlasov simulations using realistic mass ratios [e.g., Petkaki *et al.*, 2006; Petkaki and Freeman, 2008; Yoon and Lui, 2006, 2007] show that the effective collision frequencies, wave-particle interactions, previously estimated from quasi-linear theory are ~ 2 – 3 orders of magnitude too small. Furthermore, recent PIC simulations have found that wave-particle interactions can modify the macroscopic structure of collisionless shock waves [e.g., Matsukiyo and Scholer, 2006; Riquelme and Spitkovsky, 2011; Comişel *et al.*, 2011]. However, to this date, the relative contribution to energy dissipation from wave-particle interactions to the total energy dissipation budget of a collisionless shock wave has not been quantified. Therefore, we will focus on the relevance of wave-particle interactions as an energy dissipation mechanism in low-to-mid Mach number shocks. Thus, our work will focus on high-frequency electrostatic waves, specifically the ECDI waves, IAWs, and trains of ESWs because of the following: (1) previous observations [e.g., Wilson *et al.*, 2007] found the highest probability of occurrence of large-amplitude IAWs in the shock ramp; (2) several studies have documented very large amplitude electrostatic fluctuations in collisionless shock ramps [e.g., Bale *et al.*, 1998, 2002; Breneman *et al.*, 2013; Hull *et al.*, 2006; Mozer and Sundkvist, 2013; Wilson *et al.*, 2007, 2010]; and (3) theory predicts [e.g., Sagdeev, 1966; Coroniti, 1970; Tidman and Krall, 1971; Wu *et al.*, 1984; Treumann, 2009] that high-frequency electrostatic waves can be the dominant form of energy dissipation for these shocks.

In this paper we describe the first observationally quantified evidence that the microphysics (wave-particle interactions) of collisionless shock waves can dominate their macroscopic behavior (increase in entropy). More detailed discussion of the background, analysis techniques, and theoretical motivation for the results presented herein can be found in Paper I. To avoid confusion, all figures and tables from this paper will be prefaced by “II:” and those from Paper I by “I:”.

The paper is outlined as follows: Section 2 introduces the data sets used in this study; section 3 presents an example bow shock crossing at multiple scales; section 4 discusses the low- and high-frequency wave types, their relevance, and their differences; section 5 presents the quantitative estimates of the energy dissipation rates due to wave-particle interactions; and section 6 summarizes the new and important results and presents our conclusions. In addition, we included appendices to provide the reader with more detailed discussions of the high frequency wave observations (Appendix A) made by the Time History of Events and Macroscale Interactions during Substorms (THEMIS) spacecraft.

2. Data Sets

In this section we briefly introduce the THEMIS data sets used to examine the 11 bow shock crossings presented herein. Detailed discussions of the instruments, Rankine-Hugoniot analysis, critical Mach number calculations, reference frame transformations, and coordinate bases definitions can be found in Paper I.

We utilized the THEMIS fluxgate magnetometer (FGM) [Auster *et al.*, 2008] for quasi-static (DC-coupled) vector magnetic field measurements, the Search Coil Magnetometer (SCM) [Le Contel *et al.*, 2008; Roux *et al.*, 2008], and the Electric Field Instrument (EFI) [Bonnell *et al.*, 2008; Cully *et al.*, 2008] for waveform burst captures and electrostatic analyzers (ESA) [McFadden *et al.*, 2008a, 2008b] for moments of particle velocity distribution functions.

As with Paper I, we use the terms “DC-coupled” and “AC-coupled,” which are determined by whether an instrument can respond to quasi-static fields. The majority of the DC-coupled electromagnetic field measurements made by THEMIS are observed at ≤ 128 samples per second (sps). However, the electric field instrument can be DC-coupled even when sampling at ~ 8192 sps. We use the following quantity notations: Q_o is any DC-coupled quantity observed at ≤ 128 sps, δQ is any AC-coupled quantity observed at ~ 8192 sps, and $\langle Q \rangle_{\text{region}}$ is the average of any background parameter, Q , over the upstream or downstream regions. All δQ quantities that we report are measured at ~ 8192 sps with a single pole high-pass filter above ~ 10 Hz. As discussed in Paper I, Q_o and δQ are not defined with the same assumptions as in quasi-linear theory [e.g., Silin *et al.*, 2005]. We also define the following: N_i is the plasma number density; \mathbf{V}_{bulk} is the bulk flow velocity; T_i is the average ion temperature; and T_e is the average electron temperature. The data is to be presented in the following reference frames and coordinate bases (see Paper I for details): normal incidence frame (NIF); normal incidence frame coordinate basis (NCB); and field-aligned coordinates (FACs).

3. Example Bow Shock Crossing

In this section we present an example bow shock crossing. We introduce Figure II:1 and discuss its parts in multiple steps.

We examined 11 bow shock crossings with the THEMIS spacecraft. For every crossing, we removed the secondary ion populations (see Appendix C in Paper I) and electric field spikes due to photoelectron emissions and electrostatic wake effects. A quantitative comparison (e.g., see Figure I:2 in Paper I) between the electric fields observed at ~ 128 sps and those at ~ 8192 sps show that the high-frequency electric fields consistently dominate the low-frequency components or $\delta E \gg E_o$. Therefore, since we consistently observe $\delta E \gg E_o$ and the reasons outlined in Paper I, we did not focus on quasi-static electric fields.

Figure II:1 presents an example bow shock crossing observed by THEMIS-A on 26 September 2009. As shown in Table I:1, this shock had $M_f \sim 4.9$ and $\theta_{\text{Bn}} \sim 60^\circ$. Figures II:1a–II:1d show the macroscopic structure of the shock transition (left to right) from the downstream (shocked) to the upstream (not shocked). The panels are as follows: (a) $|\mathbf{B}_o|$ and its NCB components [nT, 4 sps, FGM]; (b) the plasma number density, N_i [cm^{-3} , ESAs]; (c) average electron, T_e , and one-third average ion, T_i , temperatures [eV, ESAs]; and (d) bulk flow velocity, \mathbf{V}_{bulk} [GSE, km/s, ESAs]. The center of the shock ramp is defined by the vertical green line in Figures II:1a–II:1d, and the gray-shaded region defines the time range for Figure II:1e. One can see that the shock causes significant plasma compression (i.e., $\langle N_i \rangle_{\text{down}} / \langle N_i \rangle_{\text{up}} \sim 4$), strong ion $\langle T_i \rangle_{\text{down}} / \langle T_i \rangle_{\text{up}} > 6$ and electron heating $\langle T_e \rangle_{\text{down}} / \langle T_e \rangle_{\text{up}} \gtrsim 3$, and significant deflections in \mathbf{V}_{bulk} .

The structure of this bow shock is consistent with previous observations of supercritical bow shocks. The large variability observed in $|\mathbf{B}_o|$ and \mathbf{B}_o could be explained by the following: sudden expansions and contractions of the bow shock due to changing solar wind conditions [e.g., Horbury *et al.*, 2001]; nonstationary shock reformation due to nonlinear waves [e.g., Krasnoselskikh *et al.*, 2002; Hellinger *et al.*, 2007; Lobzin *et al.*, 2007]; nonstationary shock reformation due to accumulation of reflected particles [e.g., Lembège and Savoini, 2002; Lembège *et al.*, 2009; Yang *et al.*, 2009; Su *et al.*, 2012]; or compressive nonlinear magnetic pulsations driven by the free energy from reflected ions [e.g., Scholer *et al.*, 2003; Tsubouchi and Lembège, 2004]. Regardless of their source, the large fluctuations in \mathbf{B}_o are in phase with changes in N_i and correlated with significant deflections in \mathbf{V}_{bulk} and increases in T_e and T_i . Notice that T_e (Figure II:1c) increases as the magnitude of \mathbf{V}_{bulk} (Figure II:1d) decreases and deflects. At the shock ramp, N_i and T_i increase by greater than a factor of 2 and further downstream jump by factors of 4 and 6, respectively. The apparent delayed increase in T_i with respect to T_e is partly a real phenomena and partly a consequence of the masks used in our velocity moment analysis (see Appendix C in Paper I). Therefore, the loss of bulk flow kinetic energy was partly due to a combination of ion reflection and electron heating (discussed further below). The details of the large fluctuations in \mathbf{B}_o are discussed further in section 4.1.

Possible causes for large B field (and N, V) variations:
 * Varying upstream conditions
 * Reformation due to non-linear waves
 * Reformation due to reflected part.
 * Compressive nonlinear pulsations

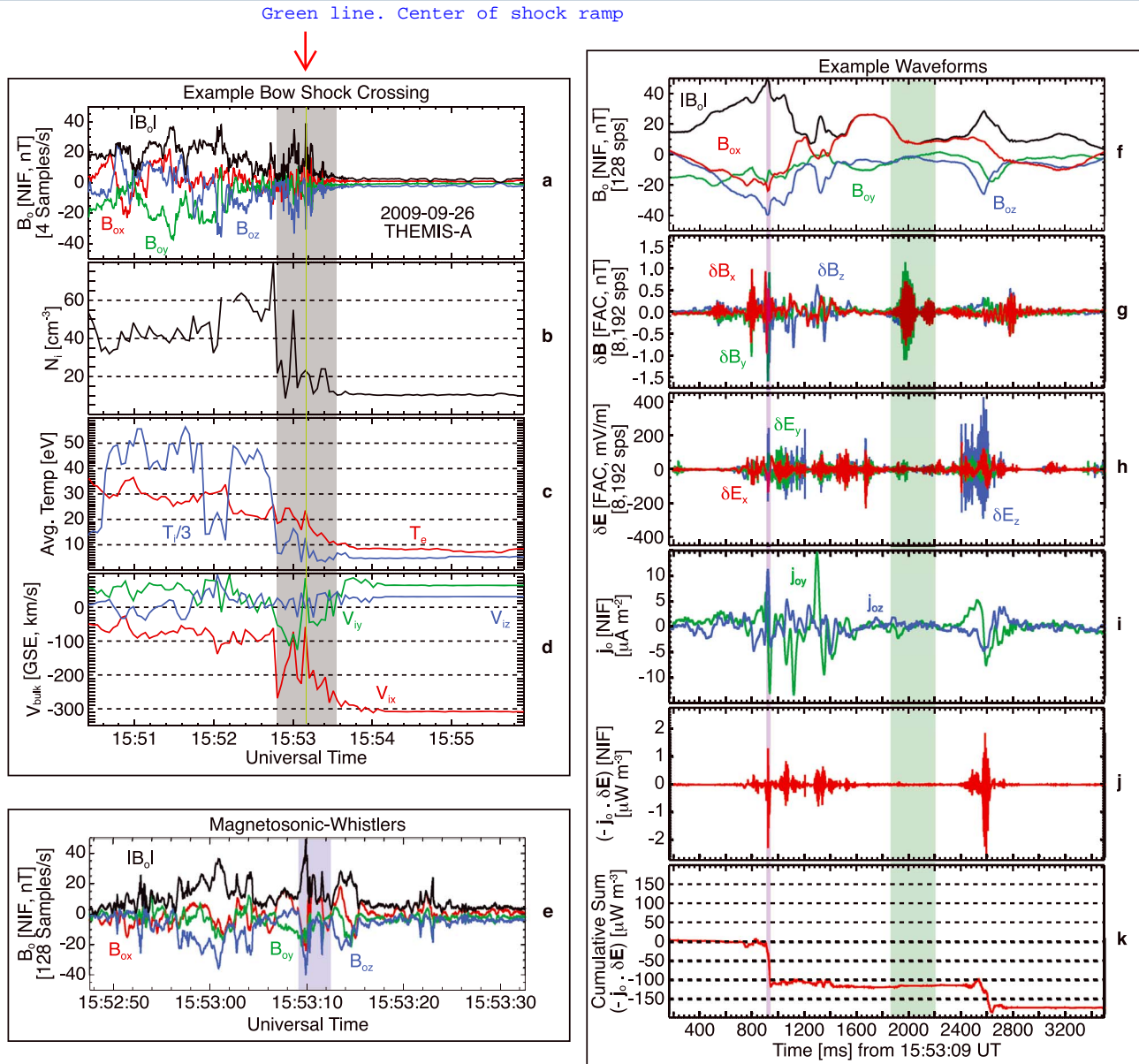
Messy B
field data

Figure II.1: (a) $|B_0|$ [nT, 4 sps, FGM] and its NCB [e.g., Scudder *et al.*, 1986] components (see Paper I for more details). (b) Plasma number density, N_i [cm^{-3} , ESAs]. (c) Average electron, T_e , and one-third average ion, T_i , temperatures [eV, ESAs]. (d) Bulk flow velocity, V_{bulk} [GSE, km/s, ESAs]. (e) $|B_0|$ [nT, 128 sps, FGM] and its NCB components. (f) $|B_0|$ [nT, 128 sps, FGM] and its NCB components. (g) δB in field-aligned coordinates (FACs) [nT, ~ 8192 sps, SCM]. (h) δE in FACs [mV/m, ~ 8192 sps, EFI]. (i) Two NCB components of the current density, j_0 [$\mu\text{A m}^{-2}$, shown at the δE time steps here]. (j) The wave (microscopic) energy dissipation rate, $(-j_0 \cdot \delta E)$ [$\mu\text{W m}^{-3}$, shown at the δE time steps here]. (k) The cumulative sum of the data in Figure II.1j. This figure delineates observations of an example bow shock crossing, showing three different time windows, observed by THEMIS-A on 26 September 2009. Figures II.1a–II.1d show a ~ 330 s window centered on $\sim 15:53:10.080$ UT (green vertical line), where the gray-shaded region indicates the ~ 45 s window for Figure II.1e and the blue-shaded region in Figure II.1e shows the ~ 3.3 s window for Figures II.1f–II.1k.

Figure II.1e shows the **higher time resolution** (~ 128 sps) data from the FGM for the ~ 45 s window corresponding to the gray-shaded region in Figures II.1a–II.1d. The ~ 128 sps FGM data (e.g., Figure II.1e) consistently showed **fluctuations not resolved** in the ~ 4 sps data (e.g., Figure II.1a). We observed that the **magnetic amplitudes in the gray-shaded region in Figure II.1a were smaller than those in Figure II.1e**. An examination of the ~ 4 sps data over the same time range as shown in Figure II.1e revealed that the **~ 4 sps data under-sampled the magnetic fluctuations** (not shown). The **fluctuations in Figure II.1e, which can occur on spatial scales much smaller than ion scales, illustrate** the highly dynamic nature of the supercritical bow shock. Only two crossings (first crossing for both 21 July 2009 and 24 October 2011) could be considered **"laminar"** in their $|B_0|$ profiles (not shown). However, **even these crossings showed small magnetic**

Those "laminar" crossings had
M_f=2.1–2.3

Laminar and turbulent shocks

Large-amplitude magnetosonic whistler waves.

10 Hz close to upper cutoff for low-frequency whistler waves.

<10 Hz

Magnetosonic whistler waves

Magnetosonic whistler waves:
 - Low frequency
 - Compressible
 - B and N fluctuations in phase
 - Frequency: f_{ci} to f_{lh}

fluctuations and/or precursor waves, whereas all other crossings showed that large-amplitude fluctuations could be described as “turbulent” shocks.

The use of higher cadence data showed that the shock transition region resembled a series of large-amplitude ($|\mathbf{B}_o|/|\mathbf{B}_o|_{up} \gtrsim 4$) nonlinear magnetic pulsations with gradient scale lengths comparable to electron gyroradii. Using methods applied in previous studies [e.g., Wilson *et al.*, 2009, 2012, 2013a, 2013b], we identified these fluctuations as magnetosonic-whistler waves (details not shown). These waves were observed in every bow shock crossing examined herein. They were primarily observed with the FGM instrument because magnetosonic-whistler waves have $f_{sc} \lesssim 10$ Hz, for typical plasma parameters. Thus, these modes were not observed in most of the high pass filtered SCM data. We discuss these modes in greater detail in section 4.1.

Figures II:1f–II:1k show the ~ 3.3 s window corresponding to the blue-shaded region in Figure II:1e. The panels are as follows: (f) $|\mathbf{B}_o|$ [nT, 128 sps, FGM] and its NCB components; (g) $\delta\mathbf{B}$ in FACs [nT, ~ 8192 sps, SCM]; (h) $\delta\mathbf{E}$ in FACs [mV/m, ~ 8192 sps, EFI]; (i) two NCB components of the current density in the NIF, \mathbf{j}_o , [$\mu\text{A m}^{-2}$]; (j) energy dissipation rates (microscopic) due to wave-particle interactions, $(-\mathbf{j}_o \cdot \delta\mathbf{E})$, [$\mu\text{W m}^{-3}$]; and (k) the cumulative sum of the data in Figure II:1j. For detailed definitions and explanations of the data in Figures II:1j–II:1k, see Paper I. We discuss Figures II:1f–II:1k in more detail in section 4.2.

Comparison between Figure II:1f and Figures II:1g–II:1k showed that there were two frequency ranges of interest. This split in frequencies was somewhat serendipitous, as the EFI instrument has an onboard high pass filter at ~ 10 Hz. Ten hertz tends to be near the upper frequency cutoff observed for the low-frequency magnetosonic whistler waves. Therefore, in the following we discuss the two frequency regimes separately and we show that the higher-frequency waves were more important for shock energy dissipation.

4. High- Versus Low-Frequency Waves

In this section we discuss low- and high-frequency waves within the context of their relative contributions to the energy dissipation due to the work done on the particles by the electromagnetic fields, $(-\mathbf{j} \cdot \mathbf{E})$. First, we discuss the lower frequency waves. Then we move on to the higher-frequency wave modes, which are the focus of this work.

4.1. Low-Frequency Waves

In this section we discuss our observations of the low-frequency (<10 Hz) electromagnetic fluctuations and their contribution to the global shock processes. We identified these modes as being primarily composed of magnetosonic-whistler waves using methods (not shown) applied in previous studies [e.g., Wilson *et al.*, 2009, 2012, 2013a, 2013b]. While lower hybrid waves have been observed in the terrestrial bow shock [e.g., Wygant *et al.*, 1987; Mellott and Greenstadt, 1988; Walker *et al.*, 2008], their amplitudes (~ 1 – 10 mV/m) were typically much smaller than the other higher-frequency modes (see section 4.2.1 and Appendix A) and were therefore not the focus of this study. First, we introduce the background and previous work related to these modes.

Magnetosonic-whistler waves are low-frequency ($f_{ci} < f_{sc} \lesssim f_{lh}$, where f_{sc} is the spacecraft frame frequency, f_{cs} is the cyclotron frequency of species s , and f_{lh} is the lower hybrid resonance frequency $= \sqrt{f_{ci}f_{ce}}$) right-hand polarized (with respect to \mathbf{B}_o) electromagnetic compressive fluctuations with magnetic fluctuations in phase with density fluctuations [e.g., Krauss-Varban and Omid, 1991; Wilson *et al.*, 2009, 2012]. Multiple magnetic fluctuations in and around collisionless shock waves have been shown to be consistent with magnetosonic-whistler waves, and these fluctuations are predicted to have multiple sources including but not limited to dispersive radiation [e.g., Tidman and Northrop, 1968; Kennel *et al.*, 1985; Krasnoselskikh *et al.*, 2002], diffuse ions [e.g., Scholer *et al.*, 2003; Tsubouchi and Lembège, 2004], reflected gyrating ion beams [e.g., Wu *et al.*, 1983; Riquelme and Spitkovsky, 2011; Comişel *et al.*, 2011], field-aligned ion beams [e.g., Akimoto *et al.*, 1993], and streaming and anisotropic electron velocity distributions [e.g., Sentman *et al.*, 1983]. Theory [e.g., Wu *et al.*, 1983; Cairns and McMillan, 2005] predicts that they can stochastically accelerate electrons parallel to \mathbf{B}_o and heat ions perpendicular to \mathbf{B}_o when propagating at highly oblique angles, which has been supported by observations [e.g., Wilson *et al.*, 2012]. Magnetosonic-whistlers are also capable of accelerating and reflecting particles when nonlinear and steepened [e.g., Wilson *et al.*, 2013b].

We observed peak amplitudes, for magnetosonic-whistler waves, as large as $B_o \gtrsim 30$ nT and $E_o \gtrsim 40$ mV/m, but typical amplitudes were smaller with $B_o \sim 1$ – 10 nT and $E_o \sim 5$ – 20 mV/m. They were observed with

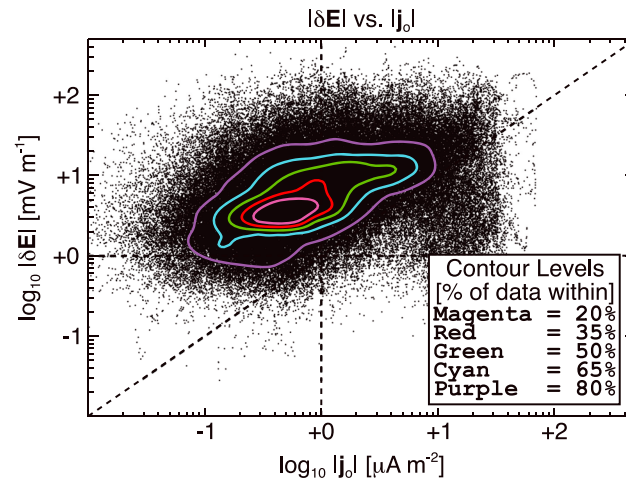


Figure 11:2. Plot showing the correlation between $|\delta\mathbf{E}|$ and $|\mathbf{j}_o|$, shown on a base 10 logarithmic scale. Black dots represent all data points examined ($>900,000$), and contours show the percentage of the data contained within. Vertical, horizontal, and diagonal dashed lines are included for reference.

see the largest electric field fluctuations simultaneously with the largest $|\mathbf{B}_o|$, consistent with previous observations [e.g., Hull *et al.*, 2006].

We observed the largest values of \mathbf{j}_o near the sharpest gradients in \mathbf{B}_o in Figures 11:1i–11:1k, which was expected due to the method used to calculate \mathbf{j}_o (for details, see section 5 in Paper I). These large \mathbf{j}_o were typically due to magnetosonic-whistler waves and were typically dominated by frequencies $\lesssim 10$ Hz. Large localized currents are important because they can act as a source of free energy for numerous plasma instabilities [e.g., Lemons and Gary, 1978].

Further examination of the data showed a positive correlation between $|\delta\mathbf{E}|$ and $|\mathbf{j}_o|$, seen in Figure 11:2. Recall that $\delta\mathbf{E}$ is measured independently from \mathbf{j}_o ; thus, the dependence is not an artifact of the calculation of \mathbf{j}_o . Increasing $|\delta\mathbf{E}|$ with increasing $|\mathbf{j}_o|$ is consistent with theories of current-driven instabilities [e.g., Sagdeev, 1966; Gary, 1981; Treumann, 2009] and previous observations [e.g., Wilson *et al.*, 2007; Breneman *et al.*, 2013]. These results are primarily for high-frequency electrostatic waves. High-frequency whistler mode waves were observed simultaneously with large-amplitude magnetosonic-whistler waves, consistent with previous observations [e.g., Hull *et al.*, 2012; Wilson *et al.*, 2013a]. Hull *et al.* [2012] argued that the magnetosonic-whistler waves produced conditions (e.g., electrons with $T_\perp/T_\parallel > 1$) conducive for the growth of higher-frequency electromagnetic whistler mode waves. However, as we discuss below, the whistler mode waves were not the focus of this study.

In summary, we believe that large-amplitude magnetosonic-whistler waves produced conditions conducive to excitation of the high-frequency electrostatic and electromagnetic waves by locally producing currents, reflected ion populations, and/or electron temperature anisotropies. Though magnetosonic-whistler waves are an important mode, they were not the focus of this study because of the following: (1) we consistently observed $\delta E \gg E_o$; (2) we consistently observed $|\mathbf{j}_o \cdot \delta\mathbf{E}| \gg |\mathbf{j}_o \cdot \mathbf{E}_o|$; and (3) we provided evidence that the magnetosonic-whistler waves did not significantly dissipate energy directly (e.g., see Figures 1:2 and 1:4 in Paper I).

4.2. High-Frequency Waves

In this section we discuss the high-frequency ($\gtrsim 10$ Hz) electromagnetic fluctuations and their contribution to the global shock processes. See Appendix A for detailed statistics and example waveforms.

All of the bow shock crossings examined had large-amplitude fluctuations in δB and δE . The data shown in Figures 11:1f–11:1k were not unusual for the bow shock crossings examined. Every bow shock crossing examined with available waveform data from THEMIS showed high-frequency ($\gtrsim 10$ Hz) large-amplitude fluctuations in both δB and δE . We observed two categories of higher-frequency waves: (1) electromagnetic

spacecraft frame frequencies satisfying $f_{ci} < f_{sc} \lesssim f_{ih}$, which was ~ 0.01 –10 Hz for observed solar wind conditions. They were also observed to have smaller contributions to the Poynting flux, S_o , than the higher-frequency waves because they had much smaller electric fields, or $E_o \ll \delta E$.

A comparison of E_o with δE for this event (not shown) showed that $E_o \ll \delta E$ was nearly always satisfied, which was consistent with observations that satisfied $|\mathbf{j}_o \cdot \delta\mathbf{E}| \gg |\mathbf{j}_o \cdot \mathbf{E}_o|$ (e.g., see Figure 1:4 in Paper I). We consistently observed peaks in δE and $(-\mathbf{j}_o \cdot \delta\mathbf{E})$ near the largest values of \mathbf{j}_o for all the bow shock crossings we examined. By definition, the largest values of \mathbf{j}_o occur near the sharpest gradients in \mathbf{B}_o . However, we occasionally find that the sharpest gradients in \mathbf{B}_o occur with peaks in $|\mathbf{B}_o|$. Thus, we often

High frequency whistler waves observed simultaneously with magnetosonic whistler waves.

Large amplitude magnetosonic whistlers cause currents and other conditions for high-frequency waves.

>10 Hz

fluctuations and (2) **electrostatic** (i.e., $(\mathbf{k} \times \delta\mathbf{E}) \sim 0$) fluctuations. The high-frequency fluctuations were composed of any combination of the following electromagnetic and electrostatic fluctuations, in no particular order: (1) **high-frequency whistler mode waves** [e.g., Hull *et al.*, 2012; Wilson *et al.*, 2013a]; (2) **trains of ESWs or electron phase space holes** [e.g., Bale *et al.*, 1998, 2002]; (3) IAWs [e.g., Fuselier and Gurnett, 1984; Balikhin *et al.*, 2005; Wilson *et al.*, 2007]; and/or (4) **ECDI** [e.g., Hull *et al.*, 2006; Wilson *et al.*, 2010].

4.2.1. Wave Properties

The **high-frequency electromagnetic waves were primarily composed of whistler mode waves**, while the **electrostatic waves were composed of combinations of ECDI, IAWs, and trains of ESWs**. In general, we observed a **decreasing δB amplitude with increasing frequency and the converse for δE** . Meaning, the **largest amplitude electric fields were found at higher frequencies**. Though the whistler mode waves produced significant contributions to δS , their contributions to $|\mathbf{j} \cdot \mathbf{E}|$ tended to be small compared to the electrostatic fluctuations. In addition, we did not observe these modes as often as the electrostatic fluctuations. Therefore, we did not focus on whistler mode waves.

ECDI, IAWs, and trains of ESWs (similar to those shown in Figures II:5–II:7) were observed in nearly every bow shock crossing we examined with not only THEMIS, but Wind [e.g., Wilson, 2010; Breneman *et al.*, 2013] and STEREO [e.g., Breneman *et al.*, 2013]. The amplitude of these fluctuations ranged from approximately tens of mV/m to >300 mV/m. The high-frequency electrostatic waves dominated the entire electric field power spectrum. They provided the largest contribution to δE and $(-\mathbf{j}_o \cdot \delta\mathbf{E})$. This point is significant because the **theory predicts that these high-frequency electrostatic waves can be the dominant form of energy dissipation in collisionless shocks** [e.g., Sagdeev, 1966; Coroniti, 1970; Tidman and Krall, 1971; Wu *et al.*, 1984; Treumann, 2009]. These **modes were observed semicontinuously from the foot through the magnetosheath**, consistent with multiple source regions (e.g., local currents) and convection of the waves into the downstream [e.g., Comișel *et al.*, 2011].

Note, ESWs can either couple to, or directly cause, the growth of IAWs [e.g., Dyrud and Oppenheim, 2006], whistler mode waves [e.g., Goldman *et al.*, 2014; Lu *et al.*, 2008; Singh *et al.*, 2001], or lower hybrid waves [e.g., Singh *et al.*, 2000]. The large magnetic fluctuations, due to magnetosonic-whistler waves, can produce strong localized currents and compress the plasma producing a temperature anisotropy. Therefore, both IAWs and high-frequency whistler mode waves observed may have been indirectly driven unstable by the low-frequency magnetosonic-whistler waves. Therefore, our THEMIS observations of combinations of ECDI, ESWs, and IAWs throughout the entire shock transition region (from foot through the magnetosheath) are consistent with simulations [e.g., Muschietti and Lembège, 2013] and previous observations [e.g., Wilson III *et al.*, 2007, 2010, 2013a; Breneman *et al.*, 2013].

5. Energy Dissipation

In this section we present our quantitative evidence that **wave-particle interactions can provide enough energy dissipation to balance the nonlinear wave steepening producing the shock**.

We examined 11 bow shock crossings with the THEMIS spacecraft (shock parameters shown in Tables I:1 and I:2 in Paper I). In every THEMIS event examined, we observed **large-amplitude electromagnetic and electrostatic fluctuations in and around the shock ramps**, with the **largest amplitudes found near the sharpest magnetic field gradients**. The long duration of the THEMIS waveform captures compared to those observed by Wind and STEREO [e.g., Breneman *et al.*, 2013] showed that these fluctuations could remain enhanced for >10 s. We also note that the **observation of these high-frequency waves was not limited to quasi-perpendicular geometry** (e.g., see Table I:1 in Paper I). Thus, we conclude that large-amplitude high-frequency electromagnetic fluctuations are ubiquitous in **quasi-parallel and quasi-perpendicular collisionless shocks**, consistent with previous results at interplanetary shocks [e.g., Wilson *et al.*, 2007] and the bow shock [e.g., Breneman *et al.*, 2013].

Due to the ubiquity of high-frequency waves in collisionless shocks, we decided to quantify the **relative contribution of these electromagnetic waves in the global energy budget** of the collisionless bow shock.

We calculate four ratios (equations (3a)–(3d) in Paper I) that compared the energy dissipation rates due to (microscopic) wave-particle interactions with the energy dissipation rates due to the change in kinetic energy density across the shock and the observed increase in entropy (macroscopic). We defined the macroscopic energy dissipation rates, $\dot{\Psi}$ and $\dot{\kappa}$ (see equations (A2) and (A3) in Paper I), as the amount of energy

δE increases with f
 δB decreases with f

High-freq electrostatic waves can dominate energy dissipation at shocks

High freq waves at both Q_{perp} and Q_{para} shocks

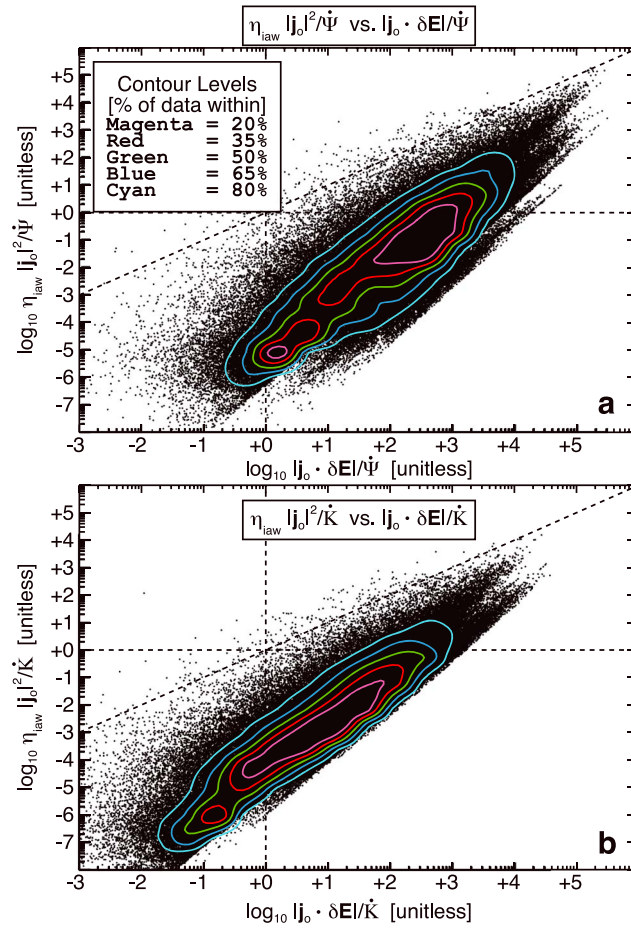


Figure II.3. The data showing that wave-particle interactions produce energy dissipation rates often exceeding the dissipation rates necessary to produce the observed increase in entropy and/or the change in kinetic energy density across the shock ramp. Black dots represent all data points examined (>900,000) and contours show the percentage of the data contained within. Vertical and horizontal dashed lines show where the plotted parameters equal unity. The diagonal dashed line shows where the plotted parameters are equal. (a) Comparison between $\mathcal{Y}_\Psi \equiv \eta_{iaw} |\mathbf{j}_o|^2 / \Psi$ and $\mathcal{R}_\Psi \equiv |\mathbf{j}_o \cdot \delta \mathbf{E}| / \Psi$ on a base 10 logarithmic scale, where η_{iaw} is the quasi-linear resistivity produced by ion-acoustic waves [e.g., Wilson et al., 2007] and $\Psi \equiv (\langle \rho \rangle_{up} \langle T \rangle_{up}) \Delta \delta / \Delta \tau$ is the energy dissipation rate needed to increase the entropy. (b) Comparison between $\mathcal{Z}_\Psi \equiv \eta_{iaw} |\mathbf{j}_o|^2 / \dot{\kappa}$ and $\mathcal{T}_\Psi \equiv |\mathbf{j}_o \cdot \delta \mathbf{E}| / \dot{\kappa}$ on the same scale as in Figure II.3a, where $\dot{\kappa} \equiv \Delta \left(\rho U_{shn}^2 \right) / (2 \Delta \tau)$ is the change in bulk flow kinetic energy density across the shock per unit time.

dissipated per unit volume per unit time necessary to increase entropy (Ψ) and transform bulk flow kinetic energy across the shock ($\dot{\kappa}$). We defined the microscopic energy dissipation rates using $(-\mathbf{j}_o \cdot \delta \mathbf{E})$ and $(-\eta_{iaw} |\mathbf{j}_o|^2)$, where the definition for η_{iaw} and the details for calculating $(-\mathbf{j}_o \cdot \delta \mathbf{E})$ are found in Paper I. Note that $(-\mathbf{j}_o \cdot \delta \mathbf{E})$ does not depend upon η_{iaw} . Rather, η_{iaw} is provided as a supplemental estimate for comparison to previous studies. Then the ratios are given by the following: $\mathcal{R}_\Psi = |\mathbf{j}_o \cdot \delta \mathbf{E}| / \Psi$; $\mathcal{T}_\Psi = |\mathbf{j}_o \cdot \delta \mathbf{E}| / \dot{\kappa}$; $\mathcal{Y}_\Psi = \eta_{iaw} |\mathbf{j}_o|^2 / \Psi$; and $\mathcal{Z}_\Psi = \eta_{iaw} |\mathbf{j}_o|^2 / \dot{\kappa}$.

Physically, \mathcal{R}_Ψ and \mathcal{Y}_Ψ are defined as ratios of the rate of work per unit volume done by the waves on the plasma to the rate of energy dissipation per unit volume necessary to produce the increase in entropy. Similarly, \mathcal{T}_Ψ and \mathcal{Z}_Ψ are ratios of the rate of work per unit volume done by the waves on the plasma to the rate of energy dissipation per unit volume necessary to produce the change in kinetic energy density. Therefore, values satisfying ≥ 1 for any ratio (\mathcal{R}_Ψ , \mathcal{Y}_Ψ , \mathcal{T}_Ψ , or \mathcal{Z}_Ψ) implied that the waves produced more work per unit volume than was necessary to regulate the global structure of the shock. Meaning, the waves could regulate the macroscopic collisionless shock dynamics for low-to-mid Mach number shocks.

Figure II.3a plots \mathcal{Y}_Ψ versus \mathcal{R}_Ψ , and Figure II.3b plots \mathcal{Z}_Ψ versus \mathcal{T}_Ψ . The plots show all high-frequency data points (>940,000) within roughly ± 10 s of the center of the shock ramp. The contours define regions containing a percentage of the total number of points shown, where the contour levels are defined in the inset box in the upper left-hand corner of Figure II.3a.

Notice that we used $|\mathbf{j}_o \cdot \delta \mathbf{E}|$ instead of $(-\mathbf{j}_o \cdot \delta \mathbf{E})$ in Figure II.3. The purpose was to illustrate the rate of work per unit volume done by the high-frequency waves. Examination of Figures II.1g–II.1k showed that the waves were bursty, short duration wave packets. Therefore, even the small amplitude periods of the high-frequency observations were capable of producing more than enough energy dissipation to regulate the global shock structure. We compared $|\mathbf{j}_o \cdot \delta \mathbf{E}|$ to $|\mathbf{j}_o \cdot \mathbf{E}_o|$ (e.g., see Figure I.4 in Paper I) and consistently found that the contribution from quasi-static fields was smaller than the high-frequency waves, typically by an order of magnitude or more. This was because we consistently observed $|\delta \mathbf{E}| \gg |\mathbf{E}_o|$.

We used $\eta_{iaw} |\mathbf{j}_o|^2$, as a supplemental estimate, in Figure II.3 to directly compare quasi-linear estimates of anomalous resistivity to actual transport effects, i.e., $|\mathbf{j}_o \cdot \delta \mathbf{E}|$. As one can see, $\eta_{iaw} |\mathbf{j}_o|^2$ was often 2 to 3

orders of magnitude smaller than $|\mathbf{j}_o \cdot \delta \mathbf{E}|$, consistent with the predictions in realistic mass ratio simulation studies [e.g., *Petkaki et al.*, 2006; *Petkaki and Freeman*, 2008; *Yoon and Lui*, 2006, 2007]. In addition, the non-linear amplitudes of the waves reduce the reliability of quasi-linear theory. Therefore, previous results using quasi-linear assumptions to approximate the relative importance of wave-particle interactions may have underestimated their contribution.

cumsum

To further quantify the importance of wave-particle interactions, we examined the cumulative sum of $(-\mathbf{j}_o \cdot \delta \mathbf{E})$, shown in Figure II:1k. This showed that the waves could contribute a net change in $(-\mathbf{j}_o \cdot \delta \mathbf{E})$, which would not have been possible if the waves were purely sinusoidal fluctuations. For sinusoidal electric field fluctuations, the oscillating electric fields could only produce periodic variations in the particle distributions. Thus, the net change observed in $(-\mathbf{j}_o \cdot \delta \mathbf{E})$ showed that the wave electric fields produced a net amount of work on the particles.

The significant, intermittent changes observed in Figure II:1k were due to the electric fields (Figures II:1h and II:5–II:7). The electric fields were observed, at times, to oscillate asymmetrically about their mean. An asymmetric oscillation could be interpreted as a net electric potential or as phase trapping by large-amplitude waves [e.g., *Kellogg et al.*, 2010]. That the high-frequency waves produced a net change in $(-\mathbf{j}_o \cdot \delta \mathbf{E})$ means that the waves lost electromagnetic energy to the particles, thus dissipating energy. Meaning, the time average of $(-\mathbf{j}_o \cdot \delta \mathbf{E})$ across the waves is not zero so that we have not neglected the restoring effects by using $|\mathbf{j}_o \cdot \delta \mathbf{E}|$.

Note that a local spike in T_e and T_i (Figure II:1c) and one of the largest deflections and decelerations in \mathbf{V}_{bulk} (Figure II:1d) occurred at the same time as the two ESWs (magenta region in Figures II:1f–II:1k and Figure II:6). The particle responses were consistent with a jump in the cumulative sum of $(-\mathbf{j}_o \cdot \delta \mathbf{E})$, which demonstrated that the waves could have been imparting momentum and energy to the particles. It is also possible that the magnetosonic-whistler wave collocated with the ESWs was causing the deceleration while the high-frequency waves produced the observed heating.

6. Discussion and Conclusions

In this section, we present our discussion and conclusions of our results.

6.1. Summary of New Results

The work presented herein can be summarized by the following points:

1. Low frequency (<10 Hz) waves.

- (i) were primarily consistent with magnetosonic-whistler waves;
- (ii) were observed ubiquitously upstream of the shock ramps;
- (iii) observed to significantly modify the shock structure, consistent with previous studies [e.g., *Horbury et al.*, 2001; *Lobzin et al.*, 2007];
- (iv) wave amplitudes were as large as $B_o \gtrsim 30$ nT and $E_o \gtrsim 40$ mV/m, but they were typically smaller with $B_o \sim 1\text{--}10$ nT and $E_o \sim 5\text{--}20$ mV/m;
- (v) however, we did not focus on them because of the following:
 - a. we consistently observed $|\mathbf{E}_o| \ll |\delta \mathbf{E}|$ and $|\mathbf{j}_o \cdot \mathbf{E}_o| \ll |\mathbf{j}_o \cdot \delta \mathbf{E}|$;
 - b. the magnetosonic-whistler waves were often observed simultaneously with large deflections and decelerations in \mathbf{V}_{bulk} , but the acceleration would be different for electrons and ions leading to relative drifts (i.e., currents);
 - c. the high correlation observed between high-frequency electrostatic fluctuations and currents, due to magnetosonic-whistler waves, suggested that the localized currents were the free energy source for the high-frequency electrostatic waves;
 - d. magnetosonic-whistler waves can only resonate with the high-energy tail of the electron distribution parallel to \mathbf{B}_o and the thermal core of the ion distribution perpendicular to \mathbf{B}_o ; and
 - e. thus, we conclude that the shock ramp and magnetosonic-whistler waves created conditions conducive to generate high-frequency waves (i.e., provide the free energy, e.g., currents, reflected ions, and/or temperature anisotropies) but do not contribute significantly to $(-\mathbf{j} \cdot \mathbf{E})$.

2. High-frequency ($\gtrsim 10$ Hz) waves.

- (i) Every bow shock crossing examined with available wave burst data from THEMIS showed large amplitude δE and δB high-frequency waves throughout the entire transition region and into the magnetosheath.
- (ii) They were found to be primarily composed of four modes: electromagnetic whistler mode waves; ion-acoustic waves (IAWs); trains of electrostatic solitary waves (ESWs); and electron cyclotron drift instability (ECDI).
- (iii) We performed an example calculation for the growth rates of the ECDI in every event to verify that the instability could reach sufficient amplitude before convecting into the downstream (see Appendix A2). Our estimates showed that the waves could saturate in much less time than is necessary to convect across the shock foot alone. Therefore, we concluded that the waves could be driven by an instability upstream of the shock ramp and still provide sufficient energy dissipation before convecting downstream.
- (iv) We also examined the spatial scale covered by a convecting particle during a collision period, determined from our lower bound estimates of the quasi-linear wave-particle collision rates in Paper I. We found that even though simulations [e.g., *Petkaki and Freeman, 2008; Yoon and Lui, 2007*] have shown these quasi-linear collision rates to be ~ 2 – 3 orders of magnitude too small, they were still large enough to allow for hundreds to thousands of collisions during the duration of a particle's trajectory through the shock. Therefore, the waves can provide sufficient effective collisions to regulate the shock.
- (v) These waves were observed to have the following:
 - a. amplitudes in excess of $\delta B \sim 10$ nT and $\delta E \sim 300$ mV/m, though they were typically observed with $\delta B \sim 0.1$ – 1.0 nT and $\delta E \sim 10$ – 50 mV/m;
 - b. $|\delta E|/(\langle |B_o| \rangle_{up})$ up to ~ 1.1 and $|\delta B|/(\langle |B_o| \rangle_{up})$ up to ~ 1.5 ;
 - c. $|\delta S|$ in excess of $\sim 2000 \mu W m^{-2}$, though typical values were between ~ 1 and $10 \mu W m^{-2}$;
 - d. v_{iaw} up to $\sim 2500 s^{-1}$, η_{iaw} up to $\sim 9000 \Omega m$, and $|\mathbf{j}_o \cdot \delta E|$ in excess of $\sim 10 \mu W m^{-3}$ (see Appendix A2); and
 - e. $>90\%$ of the time they satisfied $\mathcal{R}_\psi > 1$, $\sim 70\%$ of the time they satisfied $\mathcal{T}_\psi > 1$, $>70\%$ of the time they satisfied $\mathcal{R}_\psi > 10$, $>50\%$ of the time they satisfied $\mathcal{R}_\psi > 100$, and $>20\%$ of the time they satisfied $\mathcal{R}_\psi > 1000$ (variables defined in Paper I).
- vi. The overabundance of periods that satisfied $\mathcal{R}_\psi > 1$ and $\mathcal{T}_\psi > 1$ showed the following:
 - a. The wave dissipation rates could greatly exceed the dissipation rates necessary to balance the nonlinear steepening of the shock ramp;
 - b. The waves could provide more than enough energy dissipation to produce the observed increase in entropy across the shock ramp;
 - c. The waves could provide more than enough energy dissipation to produce the observed change in kinetic energy density across the shock ramp; and
 - d. More importantly, these results implied that the efficiency of the wave energy dissipation needed to only be, at times, $\lesssim 0.01\%$ efficient to regulate the global shock dynamics.
3. A comparison of the THEMIS observations with those from previous Wind and STEREO studies [e.g., *Breneman et al., 2013; Wilson et al., 2007, 2009, 2010; Wilson, 2010; Wilson et al., 2012, 2013a*] show the following:
 - (i) similar modes and comparable electric field amplitudes;
 - (ii) large amplitude ($\delta E \geq 100$ mV/m) high-frequency waves are ubiquitous throughout the entire bow shock transition region and the magnetosheath; and
 - (iii) both magnetosonic-whistler and high-frequency waves are observed regardless of whether the shock was quasi-parallel or quasi-perpendicular.
4. The lack of dependence on shock geometry, for magnetosonic-whistler and high-frequency wave observation, could be explained by the following:
 - (i) The presence of the free energy sources for both low- (e.g., dispersive radiation and/or reflected ions) and high-frequency (e.g., currents) modes regardless of θ_{Bn} .
 - (ii) The low-frequency magnetosonic-whistlers generate local currents [e.g., *Tidman and Northrop, 1968*] and can reflect particles when nonlinear and steepened [e.g., *Wilson et al., 2013b*]. Both can drive instabilities unstable which can radiate the high-frequency waves.
 - (iii) So long as $\theta_{Bn} > 0$, the shock ramp can source current-driven instabilities that radiate the high-frequency waves.

6.2. Discussion

The positive correlation between $|\delta\mathbf{E}|$ and $|\mathbf{j}_o|$ shown in Figure II:2 shows quantitative evidence that current-driven instabilities may be responsible for many of the observed high-frequency modes. Previous observations [e.g., Wilson *et al.*, 2007; Breneman *et al.*, 2013] indirectly support these results. It is important to note that previous studies found evidence that even more modest currents can result in similar wave modes [e.g., Malaspina *et al.*, 2013]. These results could provide predictive capabilities, which could improve the design and science return for future missions (e.g., *Solar Probe Plus*). That the high-frequency waves were often observed simultaneously with the lower frequency magnetosonic-whistler waves supports our hypothesis that these lower frequency modes dissipate energy indirectly by producing conditions conducive for the generation of the higher-frequency modes. The higher-frequency modes interact the most efficiently with their free energy source (e.g., currents) and dissipate that free energy. We provide more evidence to support this argument in the following.

Figure II:3 shows that over 90% of the observations satisfied $\mathcal{R}_\Psi > 1$ and $\sim 70\%$ of the observations satisfied $\mathcal{T}_\Psi > 1$. In fact, $>50\%$ satisfied $\mathcal{R}_\Psi > 100$ and $>20\%$ satisfied $\mathcal{R}_\Psi > 1000$. That the term $|\mathbf{j}_o \cdot \delta\mathbf{E}|$ exceeded $\dot{\Psi}$ by up to 4 orders of magnitude is important for two reasons: (1) we know that wave-particle interactions were not 100% efficient and (2) we know that the shocks were losing energy through other means (e.g., particle reflection). However, that the waves needed to only be $\sim 0.01\%$ efficient at times to regulate the global dynamics of a collisionless shock is extremely important and is discussed below.

We observed other energy dissipation mechanisms as well (e.g., particle reflection and dispersive radiation). However, as we discussed in Paper I, most of these other mechanisms result in indirect transformations of energy. For instance, we observed reflected ions in the form of gyrating beams, field-aligned beams, and/or diffuse ions [e.g., Paschmann *et al.*, 1981]. The gyrating and field-aligned beams never exceeded $\sim 5\%$ of the background density. The total relative density of the reflected ions, however, ranged from ~ 20 to 40% immediately upstream of 9 of the 11 bow shock ramps, but was ~ 1 – 2% for two crossings (see section 3.1 in Paper I). The important thing to recognize is that particle reflection is inherently reversible but can generate instabilities that radiate waves which can then dissipate energy [e.g., Matsukiyo and Scholer, 2006; Muschietti and Lembège, 2013]. We observed evidence of at least two of these instabilities: the ECDI [e.g., Wilson *et al.*, 2010; Breneman *et al.*, 2013] and the magnetic fluctuations associated with diffuse ions (which have been generalized to magnetosonic-whistler waves herein) [e.g., Wilson *et al.*, 2009, 2013b]. As we previously discussed, the latter can, in turn, produce local currents that then drive instabilities which radiate the high-frequency waves we examined herein. Therefore, we did not focus on the specifics of particle reflection as an energy dissipation mechanism because it is indirectly included as part of our estimates of $(-\mathbf{j} \cdot \mathbf{E})$.

We also did not focus on quasi-static macroscopic field effects because numerous studies have already been performed; we consistently observed $\delta E \gg E_o$ and $|\mathbf{j}_o \cdot \delta\mathbf{E}| \gg |\mathbf{j}_o \cdot \mathbf{E}_o|$, and as we discussed in Paper I, the direct effects of these fields are reversible. However, they can indirectly dissipate energy by producing unstable particle velocity distributions through mirroring and/or accelerating electrons and reflecting ions [e.g., Treumann, 2009]. Thus, since the microscopic consequences of these macroscopic fields are included in our estimates of $(-\mathbf{j} \cdot \mathbf{E})$, we did not focus on these fields.

Dispersively radiated magnetosonic-whistler waves (e.g., whistler precursors) can directly and indirectly dissipate energy. They can indirectly contribute to $(-\mathbf{j} \cdot \mathbf{E})$ by locally producing \mathbf{j}_o (e.g., due to gradients in \mathbf{B}_o) and/or \mathbf{E}_o (e.g., cause electron temperature anisotropies that excite high-frequency whistler mode waves). They can directly dissipate energy by (1) carrying momentum/energy into the upstream (i.e., their group velocity exceeds the shock velocity) and (2) scattering, heating, accelerating, or trapping particles. A previous study [e.g., Wilson *et al.*, 2012] observed large-amplitude magnetosonic-whistler precursor waves and found evidence at one interplanetary shock for parallel electron acceleration and perpendicular ion heating. However, we consistently observed $|\mathbf{j}_o \cdot \delta\mathbf{E}| \gg |\mathbf{j}_o \cdot \mathbf{E}_o|$ in this study. This, in addition to the positive correlation observed between $|\delta\mathbf{E}|$ and $|\mathbf{j}_o|$, suggests that the low-frequency magnetosonic-whistler waves are more important as an indirect rather than a direct energy dissipation mechanism.

Note that in all of these scenarios the end state is an irreversible transformation of energy at a microscopic scale through wave-particle interactions. In addition, these effects are already directly and/or indirectly included in our estimates of $(-\mathbf{j}_o \cdot \delta\mathbf{E})$. More importantly, the source of the waves does not change the fact that we consistently observe $\mathcal{R}_\Psi \gg 1$ and $\mathcal{T}_\Psi \gg 1$. It is important to note that we are not arguing that

Other dissipation mechanisms:

- * Particle reflection
- * dispersive radiation

Particle reflection is reversible but can generate waves that dissipate energy

quasi-static fields, dispersive radiation, and particle reflection are irrelevant. In fact, we argue the converse. In other words, these other mechanisms are critically important parts of a multistep chain of processes necessary for entropy production to occur in collisionless shock waves. However, that these waves can produce $\mathcal{R}_\Psi \gg 1$ and $\mathcal{T}_\Psi \gg 1$ is the most important result in our study.

These results show quantitatively that high-frequency waves play a central role in the dynamics of charged particles and energy dissipation in collisionless shock waves.

6.3. Conclusions

We present the first observationally quantified energy dissipation rates due to wave-particle interactions for 11 bow shock crossings observed by the THEMIS spacecraft. We also present the first observationally quantified evidence for current driven instabilities, showing a positive correlation between $|\delta \mathbf{E}|$ and $|\mathbf{j}_o|$. We observed that wave-particle interactions produce orders of magnitude more energy dissipation than was necessary to produce the observed increase in entropy across the shocks. Previous observational [e.g., Wilson et al., 2007, 2010, 2012] and simulation [e.g., Matsukiyo and Scholer, 2006; Muschietti and Lembège, 2013] studies only infer but do not quantify the importance of wave-particle interactions in the energy dissipation of collisionless shock waves. Other studies have focused on the effects due to quasi-static fields [e.g., Dimmock et al., 2012; Eastwood et al., 2007; Hull et al., 2001; Mitchell et al., 2012; Mitchell and Schwartz, 2014], arguing that wave-particle interactions are only of secondary importance. However, we have quantitatively shown that microscopic wave-particle interactions can regulate the macroscopic structure of low-to-mid Mach number collisionless shocks.

We conclude that wave-particle interactions have the capacity to dominate the global energy budget and control the global dynamics of low-to-mid Mach number collisionless shock waves. These results are critically important to multiple fields of research due to ubiquity of collisionless shocks and have important implications for the following (in no particular order): (1) constraints for predictions of shock wave conditions near the Sun for future missions like *Solar Probe Plus* and *Solar Orbiter*; (2) constraints on input parameters for simulations of shock wave evolution, stability, and/or propagation; (3) reconnection dynamics; (4) coronal heating; and/or (5) predictions of particle heating and acceleration in astrophysical shocks.

Appendix A: High Frequency Waves

In this appendix we present example waveform captures from the THEMIS spacecraft. Then we summarize the statistics of the wave amplitudes observed. But first, we discuss a specific limitation of quasi-linear theory and show that it is consistently violated for our observations.

If a wave, produced by an instability with a growth rate γ_k , has an associated electric field ($\delta \mathbf{E}$) parallel to its wave number (\mathbf{k}), then it can trap electrons and have an associated bounce frequency given by $\omega_B^2 = (e |k_{\parallel}| |\delta E_{\parallel}| / m_e)$ [e.g., Umeda et al., 2006]. If $\omega_B \sim \gamma_k$, then the assumption of unperturbed orbits, upon which quasi-linear theory relies, is violated. So we will compare theoretical estimates for γ_k to our numerical estimates for ω_B .

Previous studies found, for the modes we examined, that $\rho_{ci}^{-1} \lesssim k \lesssim \lambda_{De}^{-1}$, where $\rho_{ci} \equiv$ thermal ion gyroradius and $\lambda_{De} \equiv$ electron Debye length. For typical conditions near the bow shock (and in the solar wind), we have $\lambda_{De} \sim 5\text{--}20$ m, $\rho_{ci} \sim 50\text{--}200$ km. We observed $\delta E \sim 10\text{--}300$ mV/m, $B_o \sim 5\text{--}50$ nT, and $n_o \sim 5\text{--}50$ cm⁻³. For these parameters, we find $\omega_{lh} \sim 20\text{--}200$ rad/s, $\Omega_{ce} \sim 880\text{--}8800$ rad/s, $\omega_{pi} \sim 2950\text{--}9310$ rad/s (or $\Omega_{ce} \lesssim \omega_{pi}$), $\omega_{pe} \sim 1.3\text{--}4.0 \times 10^5$ rad/s, and $\omega_B \sim 10^2\text{--}10^5$ rad/s, where $\Omega_{cs} \equiv$ cyclotron frequency of species s , $\omega_{ps} \equiv$ plasma frequency of species s , and $\omega_{lh} \equiv$ lower hybrid resonance frequency. These estimates ignore the angle between \mathbf{k} and \mathbf{B}_o and $\delta \mathbf{E}$ and \mathbf{B}_o , but the correction is small for ion-acoustic and the high-frequency whistler mode waves [e.g., Fuselier and Gurnett, 1984; Breneman et al., 2013; Wilson et al., 2013a].

The typical growth rates for the observed modes are $\gamma_k \leq \omega_{lh}$ (or $\leq 20\text{--}200$ rad/s) [e.g., Lampe et al., 1972; Forslund et al., 1972; Muschietti and Lembège, 2013] for the ECDI, $\sim 10^{-2} \omega_{pi}$ (or $\sim 30\text{--}90$ rad/s) [e.g., Dum et al., 1980; Akimoto and Winske, 1985; Petkaki et al., 2006] for IAWs, $\leq 10^{-1} \Omega_{ce}$ (or $\sim 88\text{--}880$ rad/s) [e.g., Dum et al., 1980; Moreira, 1983; Baumjohann et al., 1999] for the high-frequency whistler mode waves, and $\leq 10^{-1} \omega_{pe}$ [e.g., Omura et al., 1996] for ESWs. Therefore, when the wave amplitudes are large $\omega_B \gg \gamma_k$ for the ESWs and $\gg \gamma_k$ for the ECDI, IAWs, and high-frequency whistler mode waves.

In summary, these results show that the approximations for quasi-linear theory are probably invalid and any results based upon this theory should be used with care.

A1. THEMIS Examples

The first waveform we present is the **electromagnetic whistler mode wave**. Whistler mode waves have been observed as a **right-hand** polarized (with respect to \mathbf{B}_0) electromagnetic mode propagating at small angles from \mathbf{B}_0 with rest frame frequencies $f \leq f_{ce}/2$ [e.g., Hull et al., 2012; Wilson et al., 2013a]. They have been observed **in and around the ramp region and downstream** of collisionless shocks. The source of these modes can be an electron temperature anisotropy ($T_{\perp}/T_{\parallel} > 1$) instability [e.g., Kennel and Petschek, 1966], an electron heat flux instability [e.g., Gary et al., 1994], or nonlinear wave decay [e.g., Goldman et al., 2014; Lu et al., 2008; Singh et al., 2001]. These modes are important because they are thought to regulate the electron heat flux and electron halo temperature anisotropy in the solar wind. At shocks, these modes are important because they can efficiently **exchange energy/momentum between electrons and ions and can couple to multiple wave modes** [Dyrud and Oppenheim, 2006].

High frequency whistler mode waves are electromagnetic fluctuations with frequency peaks between f_{lh} and the electron cyclotron frequency, f_{ce} , or $f_{lh} \ll f_{sc} \leq f_{ce}$. We observed these waves to have large amplitudes with δB and δE up to ~ 2 nT and ~ 30 mV/m, respectively, but they typically have $\delta B \lesssim 0.5$ nT and $\delta E \lesssim 10$ mV/m. While they had large δB , their **amplitudes were always smaller than the lower frequency magnetosonic-whistler waves**. Thus, the **magnetic field spectrum showed a decreasing trend with increasing frequency**. Though they produced significant contributions to δS , they were observed less often and their contribution to $|\mathbf{j}_0 \cdot \delta \mathbf{E}|$ was often much smaller (e.g., see Figures II:1j–II:1k and Paper I) than the **electrostatic modes** because (1) they had much smaller δE and (2) they were not typically observed with large currents. Therefore, we did not focus on these modes.

Figure II:4 shows an example of a typical high-frequency ($f_{lh} \ll f < f_{ce}$) electromagnetic whistler mode wave. The left-hand column of the figure shows $\delta \mathbf{B}$ in FACs with corresponding amplitudes defined by the black arrows, where the first two rows are the perpendicular components and the last row is the parallel component. The right-hand column shows the corresponding wavelet transforms, shown on the same color-scale range defined by the color bar at the bottom of the right-hand column. Previous observations of these modes found that they propagate at small angles relative to \mathbf{B}_0 [e.g., Hull et al., 2012; Wilson et al., 2013a], as illustrated by the relatively small ratios of $\delta B_{\parallel}/\delta B_{\perp}$ in Figure II:4. The waves were observed as short duration (\sim few tens to hundreds of milliseconds) bursty wave packets that could have large amplitudes ($\delta B > \text{few nT}$). The corresponding electric field amplitudes for this example (see Figure II:1h) ranged from \sim few mV/m up to ~ 30 mV/m.

Their ability to efficiently exchange energy/momentum between electrons and ions and couple to multiple wave modes provide multiple pathways to **transform energy from electromagnetic to kinetic or vice versa**. However, it has been shown that these modes are important for regulating the electron heat flux and temperature anisotropies in the halo electrons [e.g., Gary et al., 1994; Wilson et al., 2013a]. This study is focused on the quantification of the energy dissipation in collisionless shock waves due to wave-particle interactions. Therefore, because whistler mode waves were observed to have much smaller values of $|\mathbf{j}_0 \cdot \delta \mathbf{E}|$ than the electrostatic modes, we did not focus on these waves.

The **high-frequency electrostatic waves** were composed of combinations of **ECDI, IAWs, and trains of ESWs**. **Ignoring the high-frequency whistler mode waves**, there was **typically a large frequency gap between the low-frequency magnetosonic-whistler waves and the higher-frequency electrostatic waves**. Their peak values of δE typically occurred at spacecraft frame frequencies between the ion (f_{pi}) and electron plasma frequency (f_{pe}), or $f_{pi} \leq f_{sc} \leq f_{pe}$. Though we refer to these modes as electrostatic, they had $\delta B \neq 0$, thus $\delta S \neq 0$. They had electric field amplitudes $\delta E \gtrsim 300$ mV/m, but more typical values were $\delta E \sim 10$ – 50 mV/m.

The first electrostatic waves we discuss are IAWs. IAWs are linearly polarized electrostatic wave modes with wavelengths $\lambda \gtrsim 2\pi\lambda_{De}$ and rest frame frequencies $\omega_0 \lesssim \omega_{pi}$ [e.g., Gurnett et al., 1979a, 1979b; Fuselier and Gurnett, 1984; Balikhin et al., 2005; Wilson et al., 2007], where λ_{De} is the electron Debye length and ω_{ps} is the plasma frequency of species s . In the solar wind, their **spacecraft frame frequencies are Doppler-shifted up to ~ 1 – 10 kHz**. IAWs were originally predicted [e.g., Vedenov, 1963; Sagdeev, 1966; Gary, 1981] to play an important role in collisionless shocks by providing sufficient resistivity to regulate the shock. Consistent with this theory, previous observations have shown that the **ramp region of collisionless shocks are dominated**

Electromagnetic whistler mode wave

$f_{lf} \ll f < f_{ce}$

High frequency electrostatic:
 * Electron cyclotron drift
 instability waves
 * Ion acoustic waves
 * Electrostatic waves
 * High-freq whistler mode

$f_{pi} < f_{pe}$

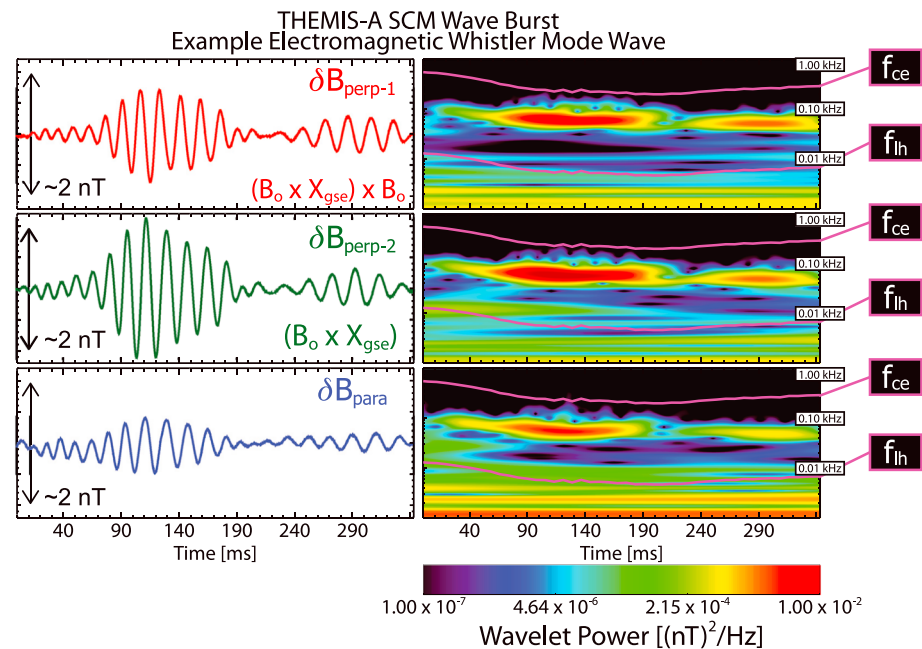


Figure II.4. An example waveform showing **high-frequency whistler mode waves** observed by the SCM instrument in wave burst mode for a ~ 340 ms time window near the shock ramp on 26 September 2009 at $\sim 15:53:10.860$ UT (gray shaded timespan in Figures II:1f–II:1k). The right-hand column shows the corresponding wavelet transforms [Torrence and Compo, 1998] with the frequency on a logarithmic scale from ~ 1 to 1000 Hz. **Two magenta lines are shown in the wavelets corresponding to f_{lh} and f_{ce} .**

by large-amplitude IAWs [e.g., Wilson et al., 2007]. IAWs have been predicted to create high-energy tails in ion distributions and flattops in electron distributions [Dum et al., 1974].

Figure II:5 shows an example of Doppler-shifted IAWs. The figure shows δE in FACs, otherwise the format is similar to Figure II:4. The wave is observed just downstream of the shock ramp in the magnetosheath. The local particle density is $\sim 8\text{--}10\text{ cm}^{-3}$ corresponding to $f_{pi} \sim 590\text{--}660$ Hz and the angle between \mathbf{B}_0 and $\mathbf{V}_{bulk} \sim 82^\circ$. Thus, the wave should show minimal Doppler effects because its **wave vector is roughly along \mathbf{B}_0** , from observation that $\delta E_{||} \gg \delta E_{\perp}$ and the mode is primarily electrostatic. Thus, the spacecraft frame frequency should be roughly the same as the plasma frame frequency for this example. Previous studies [e.g., Gurnett et al., 1979a, 1979b; Fuselier and Gurnett, 1984; Balikhin et al., 2005; Wilson et al., 2007] showed that $f < f_{pi}$, which is consistent with this example.

The next electrostatic waves we discuss are ESWs. ESWs are observed as **bipolar electric field fluctuations parallel to \mathbf{B}_0 and monopolar perpendicular to \mathbf{B}_0** and have been found to be consistent with BGK electron **phase space holes**. ESWs can be driven unstable by electron beams [e.g., Cattell et al., 2005; Ergun et al., 1998; Franz et al., 2005], modified two-stream instability (MTSI) [e.g., Matsukiyo and Scholer, 2006], or the produce of high-frequency wave decay [e.g., Singh et al., 2000]. ESWs are one of the more important modes at collisionless shocks because they can trap incident electrons [e.g., Dyrud and Oppenheim, 2006; Lu et al., 2008], **heat ions** [e.g., Ergun et al., 1998], and/or couple to (or directly cause) the growth of IAWs [e.g., Dyrud and Oppenheim, 2006], whistler mode waves [e.g., Goldman et al., 2014; Lu et al., 2008; Singh et al., 2001], lower hybrid waves [e.g., Singh et al., 2000], and/or electron acoustic waves [e.g., Matsukiyo and Scholer, 2006]. Because ESWs act like clumps of positive charge, they can **efficiently scatter incident ions**. Previous observations have shown that a train of ESWs can increase $T_{\perp,i}$ by as much as the total initial thermal energy [Ergun et al., 1998].

Figure II:6 shows an example of **two large-amplitude ESWs** observed at the peak of the shock overshoot (see magenta region in Figures II:1f–II:1k). The low-frequency ($\lesssim 40$ Hz) signal, on which the ESWs bipolar signatures were superposed, is most likely artificial (e.g., remnant spin tone) and should be ignored. The fluctuations have waveform and frequency spectrum characteristics similar to previous observations of ESWs [e.g., Bale et al., 1998; Wilson et al., 2007, 2010]. ESWs are often too short in duration for many electric field

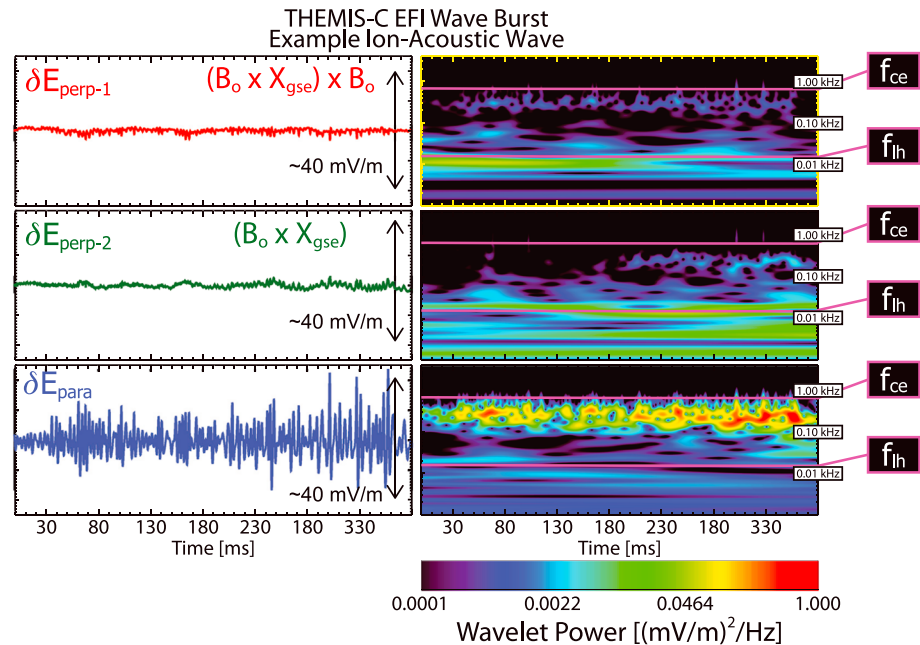


Figure II:5. An example waveform showing IAWs observed by the EFI instrument in wave burst mode for a ~ 380 ms time window near the shock ramp on 21 July 2009 at $\sim 19:23:21.420$ UT. The format is similar to that of Figure II:4 except that electric fields are shown and the frequency ranges from ~ 1 to 4000 Hz.

detectors to resolve. Even at ~ 8192 sps, these two examples were nearly under-sampled. The same fluctuations observed at $\sim 16,384$ sps (not shown), by comparison, show smooth and continuous bipolar pulses in δE_{\parallel} .

Finally, we discuss the electric field observations consistent with those expected from the ECDI. The ECDI radiates waves consistent with a mixture of Doppler-shifted IAWs and electron Bernstein modes (seen as integer and half-integer harmonics of f_{ce}), though, for brevity, we will refer to the wave observations as just the ECDI. They are driven unstable by the relative drift between incident electrons and shock-reflected ions [e.g., Matsukiyo and Scholer, 2006; Muschietti and Lembège, 2013]. Very few observations have been made of these modes near collisionless shocks. Hull *et al.* [2006], in a bow shock study, described nonlinear fluctuations that they identified as electrostatic IAWs. Wilson *et al.* [2010] observed similar fluctuations at an interplanetary shock and argued that they were consistent with the ECDI. More recently, Breneman *et al.* [2013] examined similar fluctuations in multiple bow shock crossings with the Wind and STEREO spacecraft identifying them as ECDI. However, Breneman *et al.* [2013] noted that the distinction between IAWs and ECDI can often be difficult.

ECDI-driven waves are important for shock physics because they are capable of resonantly interacting with the bulk of the ion distribution and preferentially heating the electrons perpendicular to \mathbf{B}_0 [Forslund *et al.*, 1970, 1972; Lampe *et al.*, 1972]. More recent work has shown that the ECDI can produce a suprathermal tail on the ion distribution and can strongly heat the electrons [Muschietti and Lembège, 2013]. This is accomplished through the following: (1) the ECDI is excited at multiple harmonics of f_{ce} by removing bulk kinetic energy from the reflected ions; (2) these electrostatic fluctuations interact with the electrons and trap some of the reflected ions; (3) the wave amplitudes decrease, where higher harmonics experience more damping than lower harmonics; thus allowing (4) the waves to irreversibly exchange energy and momentum between particle species.

Figure II:7 shows an example ECDI waveform observed by THEMIS-B near the bow shock ramp on 13 July 2009. Overlaid on the wavelets are color-coded lines showing integer and half-integer harmonics of f_{ce} . The fluctuations have waveform and frequency spectrum characteristics similar to previous observations [e.g., Hull *et al.*, 2006; Wilson *et al.*, 2010]. One can see, however, that the fluctuations are not simple Doppler-shifted IAWs (compared to the waveform in Figure II:5). Their properties include (1) asymmetric oscillation of $\delta \mathbf{E}$ about a mean value (i.e., may imply a net potential drop); (2) significant amplitudes

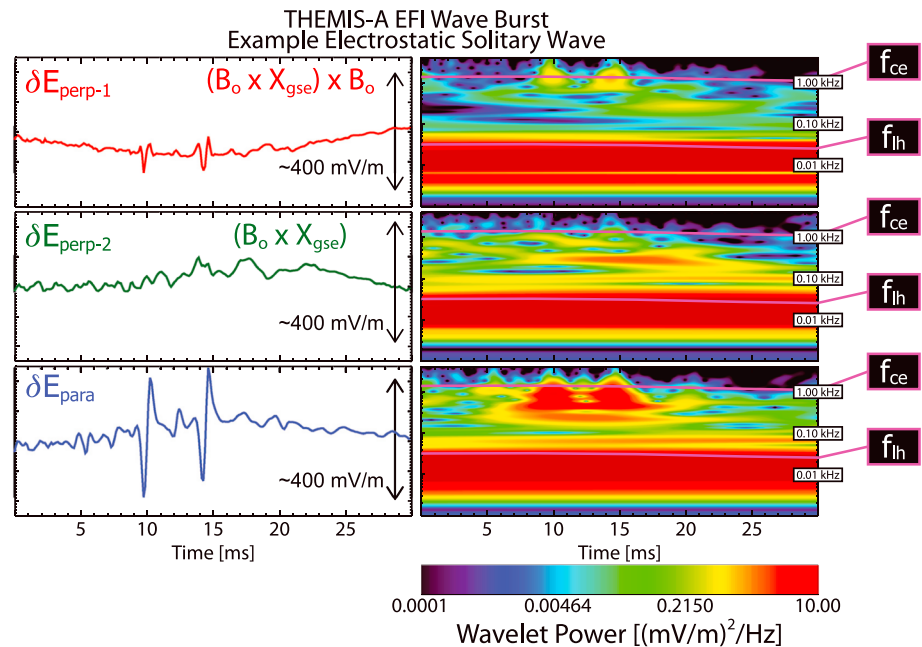


Figure II.6. An example waveform showing two **ESWs** observed by the EFI instrument in wave burst mode for a ~ 30 ms time window near the shock ramp on 26 September 2009 at $\sim 15:53:09.910$ UT (magenta shaded timespan in Figures II:1f–II:1k). The format is similar to that of Figure II:5.

perpendicular to B_o ; (3) significant amplitudes parallel to the shock normal vector (not shown); and (4) power focused at integer and half-integer harmonics of f_{ce} .

The study by *Muschiatti and Lembège* [2013] focused on the effects of the ECDI in a perpendicular shock. We observed that the waves predominantly observed include the ECDI as well as IAWs and ESWs. While we observed ECDI in each crossing, the majority of the electrostatic waves were more consistent with IAWs and ESWs. *Muschiatti and Lembège* [2013] ran an example simulation to compare the evolution of the ECDI and IAWs. They found that at late times in their simulations, the ECDI and IAWs had very similar power spectrums (ignoring the peaks due to the Bernstein modes in the ECDI). The only differences were in the wave polarization and their respective effects on the particle distributions. The IAWs in their simulation began to form electron phase space holes at later times.

We should note that some recent simulations argue that the ECDI is less important than the modified two-stream instability [e.g., *Umeda et al.*, 2012]. The fluctuations associated with this instability would be observed at much lower frequencies (e.g., f_{ih}) than those associated with the ECDI. It may be that some of the low-frequency fluctuations, included in our broad generalization as magnetosonic whistler modes, are due to the modified two-stream instability. However, this is beyond the scope of this paper.

The similarity in the power spectrums for the ECDI and IAWs found by *Muschiatti and Lembège* [2013] should be expected since the ECDI is a series of electron Bernstein modes coupled to Doppler-shifted IAWs. However, it adds difficulty to the unique identification of each mode. Moreover, *Muschiatti and Lembège* [2013] found that the higher harmonics damped out leaving only the fundamental after sufficient time. The result was a well-defined peak near f_{ce} and a broad, weaker spectrum at higher frequencies. At this point, the simulated ECDI power spectrum looked very similar to the simulated IAW power spectrum. Thus, it was not surprising that we identified fluctuations consistent with both the ECDI and IAWs.

A2. Wave Statistics

In this appendix we present a summary of our statistical analysis of the wave amplitudes to help illustrate their importance, large amplitude, and relevance to collisionless shock physics.

For events where the EFI was sampling at $\sim 16,384$ sps while the SCM was sampling at ~ 8192 sps, we down-sampled the EFI to the SCM time steps, after calibration. Then these two fields, $\delta \mathbf{E}$ and $\delta \mathbf{B}$, were used to estimate the Poynting flux, $\delta \mathbf{S} = (\delta \mathbf{E} \times \delta \mathbf{B})/\mu_o$, in temporal and frequency space. $\delta \mathbf{S}$ was calculated after

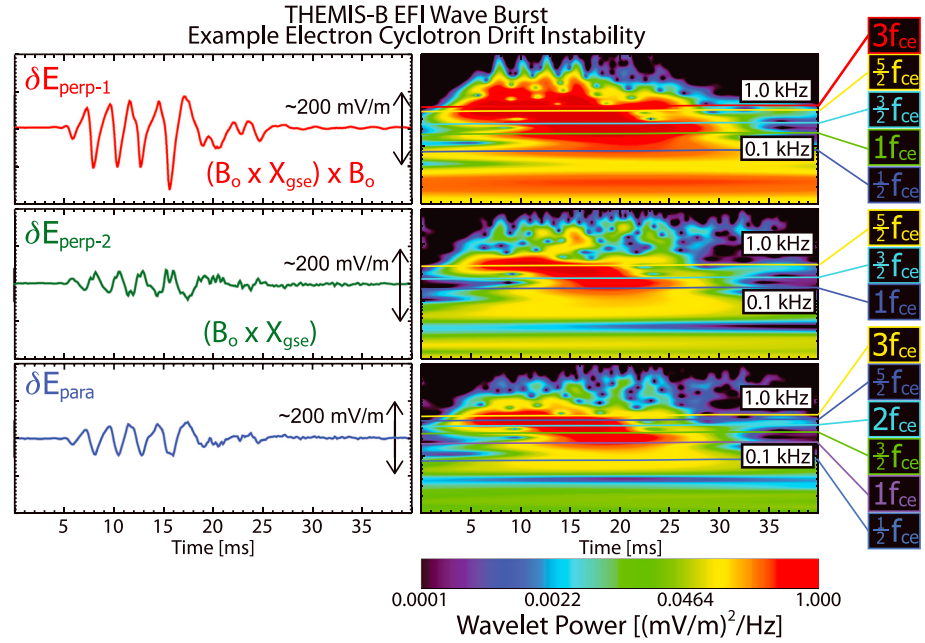


Figure II.7. An example waveform showing **ECDI-driven** waves observed by the EFI instrument in wave burst mode for a 40 ms time window near the shock ramp on 13 July 2009 at ~08:59:52.890 UT. The format is similar to Figure II.5 except that the frequency ranges from ~10 to 4000 Hz, and multiple integer and half-integer harmonics of f_{ce} are shown in the wavelets.

both $\delta \mathbf{E}$ and $\delta \mathbf{B}$ were filtered and after each was transformed or rotated into the desired reference frame or coordinate basis, respectively.

From our THEMIS bow shock crossings, we have 940,734 data points up-sampled to the $\delta \mathbf{E}$ time stamps (justification given in section 5 in Paper I). From those data points, we found the statistics shown in Table II.1. The columns are defined in the following order: (1) parameter name and units; (2) minimum value; (3) maximum value; (4) mean or average value, $\langle X \rangle$; (5) standard deviation, σ_x ; (6) standard deviation of the mean, σ_x/\sqrt{N} ; and (7) the number of points used, N . In Table II.1 we use the following definitions for brevity: $|\delta \tilde{\mathbf{S}}| \equiv$ frequency summed $\delta \mathbf{S}$, $\mathfrak{B} \equiv |\delta \mathbf{B}|/|\mathbf{B}_o|_{up}$, $\mathfrak{b} \equiv |\mathbf{B}_o|/|\mathbf{B}_o|_{up}$, $\mathcal{W}_B \equiv |\delta \mathbf{B}|^2/(2\mu_o)$, $\mathcal{W}_E \equiv \epsilon_o |\delta \mathbf{E}|^2/2$, $\mathfrak{C} \equiv |\delta \mathbf{E}|/(c |\mathbf{B}_o|_{up})$, $S_\eta \equiv \eta_{iaw} |\mathbf{j}_o|^2$, $\mathfrak{R}_\eta \equiv |\mathbf{j}_o \cdot \delta \mathbf{E}|$, $\mathcal{R}_\Psi \equiv |\mathbf{j}_o \cdot \delta \mathbf{E}|/\Psi$, and $\mathcal{Y}_\Psi \equiv \eta_{iaw} |\mathbf{j}_o|^2/\Psi$ (defined in Paper I).

The purpose of calculating $|\delta \tilde{\mathbf{S}}|$ was to examine the upper bound on $\delta \mathbf{S}$. This calculation decomposed the signal into frequency space prior to performing the cross product, which ensured that matching frequency components were multiplied together. However, $|\delta \tilde{\mathbf{S}}|$ is positive definite even if $\delta \mathbf{S}$ varies periodically.

Table II.1. Wave Property Statistics

Type	Minimum	Maximum	$\langle X \rangle$	σ_x	σ_x/\sqrt{N}	N
$ \delta \mathbf{E} $ [mV m ⁻¹]	1.50×10^{-02}	$2.99 \times 10^{+02}$	$1.20 \times 10^{+01}$	$1.75 \times 10^{+01}$	1.83×10^{-02}	907,084
$ \delta \mathbf{B} $ [nT]	9.72×10^{-05}	$1.00 \times 10^{+01}$	2.02×10^{-01}	4.11×10^{-01}	4.23×10^{-04}	940,732
$ \delta \mathbf{S} $ [μ W m ⁻²]	3.20×10^{-05}	$2.08 \times 10^{+03}$	$2.54 \times 10^{+00}$	$1.39 \times 10^{+01}$	1.46×10^{-02}	907,146
$ \delta \tilde{\mathbf{S}} $ [μ W m ⁻²]	2.89×10^{-03}	$2.89 \times 10^{+03}$	$1.58 \times 10^{+01}$	$6.91 \times 10^{+01}$	7.27×10^{-02}	903,153
\mathfrak{B} [unitless]	4.74×10^{-05}	$1.45 \times 10^{+00}$	2.65×10^{-02}	3.77×10^{-02}	3.89×10^{-05}	940,732
\mathfrak{b} [unitless]	1.92×10^{-01}	$2.22 \times 10^{+01}$	$4.57 \times 10^{+00}$	$3.54 \times 10^{+00}$	3.65×10^{-03}	940,734
\mathfrak{C} [unitless]	3.66×10^{-05}	$1.09 \times 10^{+00}$	9.20×10^{-03}	1.85×10^{-02}	1.94×10^{-05}	907,119
\mathcal{W}_B [μ W m ⁻³]	3.76×10^{-15}	3.99×10^{-05}	8.33×10^{-08}	6.00×10^{-07}	6.19×10^{-10}	940,732
\mathcal{W}_E [μ W m ⁻³]	9.94×10^{-16}	3.96×10^{-07}	1.99×10^{-09}	9.35×10^{-09}	9.82×10^{-12}	907,084
v_{iaw} [coll. s ⁻¹]	2.32×10^{-06}	$2.48 \times 10^{+03}$	$5.15 \times 10^{+00}$	$3.06 \times 10^{+01}$	3.21×10^{-02}	907,084
η_{iaw} [Ω m]	3.12×10^{-05}	$9.38 \times 10^{+03}$	$1.59 \times 10^{+01}$	$1.07 \times 10^{+02}$	1.13×10^{-01}	907,084
\mathfrak{R}_η [μ W m ⁻³]	2.10×10^{-09}	$1.08 \times 10^{+01}$	2.34×10^{-02}	1.13×10^{-01}	1.19×10^{-04}	907,084
S_η [μ W m ⁻³]	3.54×10^{-14}	$3.46 \times 10^{+00}$	8.61×10^{-04}	2.03×10^{-02}	2.13×10^{-05}	907,084
\mathcal{Y}_Ψ [unitless]	9.06×10^{-11}	$3.98 \times 10^{+05}$	$5.71 \times 10^{+01}$	$1.31 \times 10^{+03}$	$1.38 \times 10^{+00}$	907,084
\mathcal{R}_Ψ [unitless]	5.36×10^{-06}	$6.69 \times 10^{+05}$	$1.54 \times 10^{+03}$	$6.02 \times 10^{+03}$	$6.32 \times 10^{+00}$	907,084

One can see that there were a wide range of wave amplitudes with high-frequency (i.e., AC-coupled) electric and magnetic fields exceeding 250 mV/m and 10 nT, respectively. The magnetic fluctuations relative to an upstream averaged magnetic field magnitude, $|\mathbf{B}_o|/\langle|\mathbf{B}_o|\rangle_{\text{up}}$ (FGM) were found to easily exceed ~ 10 and $|\delta\mathbf{B}|/\langle|\mathbf{B}_o|\rangle_{\text{up}}$ (SCM) could exceed ~ 1 . The electric fluctuations (EFI) $|\delta\mathbf{E}|/(c\langle|\mathbf{B}_o|\rangle_{\text{up}})$ can exceed ~ 1 as well. The peak values for $|\delta\mathbf{S}|$ and $|\delta\tilde{\mathbf{S}}|$, at times, exceeded $2000 \mu\text{W m}^{-2}$. These values are incredibly large, comparable to the energy fluxes needed to drive the terrestrial aurora [e.g., Angelopoulos *et al.*, 2002; Wygant *et al.*, 2000] and larger than the largest values observed for whistler mode waves in the radiation belts [see, e.g., Wilson *et al.*, 2011]. Such large energy fluxes illustrate the capacity of these high-frequency waves to dominate the energy dissipation in collisionless shock waves.

To verify that these fluctuations could indeed result from instabilities, we calculated an example growth rate estimate for the ECDI [e.g., see Muschietti and Lembège, 2013, equation (8)]. We needed to confirm that the waves can grow to sufficient amplitudes in less time than was necessary to convect across the shock foot. The physically significant time scale was the lower hybrid resonance period, $\tau_{\text{lh}} (= 2\pi/\omega_{\text{lh}})$, where $\omega_{\text{lh}} = (\Omega_{\text{ci}}\Omega_{\text{ce}})^{1/2}$. The growth rate of the ECDI for large wavelengths is $\gamma_{\text{max}} \sim (M_i/m_e)^{3/4} (\alpha/8\pi)^{1/4} \Omega_{\text{ci}}$, where α is the ratio of ion beam to total ion density. We defined the following scale lengths: a convection scale length, $L_{\text{conv}} \equiv V_e \tau_{\text{lh}}$ (where V_e is the incident electron speed in the shock frame); and a scale length for the shock foot, $L_f \equiv U_{\text{shn}}/\langle\Omega_{\text{ci}}\rangle_{\text{up}}$. Physically, ratios that satisfy $L_{\text{conv}}/L_f < 1$ imply that the waves could grow to sufficient amplitudes before convecting across the shock foot.

To further support this, we estimate the scale length traversed during a typical collision frequency interval, $L_{\text{wp}} \equiv U_{\text{shn}}/v_{\text{iaw}}$, where v_{iaw} is the wave-particle collision rate for IAWs defined in equation (B2a) of Paper I. Therefore, we will have several thousand estimates for L_{wp} per shock crossing. If we estimate an average collision rate for all points in one shock crossing, then we find a range of $0.2 \text{ \#}/s \lesssim \langle v_{\text{iaw}} \rangle \lesssim 22 \text{ \#}/s$, with peak values for all crossing $\geq 140 \text{ \#}/s$. For one event, v_{iaw} exceeded $3800 \text{ \#}/s$. For wave-particle interactions to be relevant, one requires that L_{wp} be smaller than L_{foot} and/or the shock thickness, $L_{\text{sh}} = V_{\text{shn}} \Delta\tau$, where $\Delta\tau \equiv$ shock ramp duration. For the 11 bow shock crossings examined, we have $10^{-3} \lesssim L_{\text{wp}}/L_{\text{sh}} \lesssim 10^5$ and $10^{-5} \lesssim L_{\text{wp}}/L_{\text{foot}} \lesssim 10^4$. Note that $L_{\text{wp}}/L_{\text{sh}} \lesssim 1$ for at least 140 samples (i.e., $\delta\mathbf{E}$ sample periods or ~ 17 ms) in every shock and $L_{\text{wp}}/L_{\text{foot}} \lesssim 1$ for at least 2500 samples (or ~ 305 ms) in every shock. In 9 of the 11 shock crossings, $L_{\text{wp}}/L_{\text{foot}} \lesssim 1$ at for at least 30% of the total samples per crossing, even though simulations have shown that v_{iaw} is ~ 2 – 3 orders of magnitude too small [e.g., Petkaki *et al.*, 2006; Petkaki and Freeman, 2008; Yoon and Lui, 2006, 2007]. However, it is still large enough to allow the waves to produce hundreds to thousands of collisions before a particle traversed the foot and/or shock ramp.

There are a few points to emphasize when considering these results:

1. Recall that each shock crossing has several seconds of $\delta\mathbf{E}$, much of which is small in amplitude because the large \mathbf{j}_o values are highly localized (e.g., see Figures I:3 and II:1);
2. These estimates ignore particle gyration and the possibility for particle reflection or trapping;
3. The quasi-linear estimates of v_{iaw} , used for supplemental purposes in our studies, have been shown to be ~ 2 – 3 orders of magnitude too small [e.g., Petkaki *et al.*, 2006; Petkaki and Freeman, 2008; Yoon and Lui, 2006, 2007]; and
4. The dissipation estimates derived from v_{iaw} were ~ 2 – 3 orders of magnitude smaller than those derived from $(-\mathbf{j}_o \cdot \delta\mathbf{E})$.

For the THEMIS events examined herein, we found $0.0007 \lesssim L_{\text{conv}}/L_f \lesssim 0.14$. Therefore, the waves should convect distances much less than the scale of the shock foot before growing to substantial amplitudes. As we discussed previously, we observed large amplitude waves throughout the entire transition region for every bow shock crossing.

References

- Akimoto, K., and D. Winske (1985), Ion-acoustic-like waves excited by the reflected ions at the Earth's bow shock, *J. Geophys. Res.*, **90**(A12), 12,095–12,103, doi:10.1029/JA090iA12p12095.
- Akimoto, K., D. Winske, S. P. Gary, and M. F. Thomsen (1993), Nonlinear evolution of electromagnetic ion beam instabilities, *J. Geophys. Res.*, **98**, 1419–1433, doi:10.1029/92JA02345.
- Angelopoulos, V., J. A. Chapman, F. S. Mozer, J. D. Scudder, C. T. Russell, K. Tsuruda, T. Mukai, T. J. Hughes, and K. Yumoto (2002), Plasma sheet electromagnetic power generation and its dissipation along auroral field lines, *J. Geophys. Res.*, **107**(A8), 1181, doi:10.1029/2001JA900136.
- Auster, H. U., et al. (2008), The THEMIS fluxgate magnetometer, *Space Sci. Rev.*, **141**, 235–264, doi:10.1007/s11214-008-9365-9.

Acknowledgments

We would like to thank A.F.- Viñas, D. Bryant, D.A. Roberts, R.T. Wicks, R. Lysak, and M.L. Goldstein for useful discussions of the fundamental physics involved in our study. The work was partially supported by Wind MO&DA grants. The French involvement (SCM instruments) on THEMIS are supported by CNES and CNRS-INSU. The data used in this paper and the associated calibration software can be found at <http://themis.ssl.berkeley.edu/index.shtml>.

Yuming Wang thanks the reviewers for their assistance in evaluating this paper.

- Bale, S. D., P. J. Kellogg, D. E. Larson, R. P. Lin, K. Goetz, and R. P. Lepping (1998), Bipolar electrostatic structures in the shock transition region: Evidence of electron phase space holes, *Geophys. Res. Lett.*, **25**, 2929–2932, doi:10.1029/98GL02111.
- Bale, S. D., A. Hull, D. E. Larson, R. P. Lin, L. Muschietti, P. J. Kellogg, K. Goetz, and S. J. Monson (2002), Electrostatic turbulence and Debye-scale structures associated with electron thermalization at collisionless shocks, *Astrophys. J.*, **575**, L25–L28, doi:10.1086/342609.
- Balikhin, M., S. Walker, R. Treumann, H. Alleyne, V. Krasnoselskikh, M. Gedalin, M. Andre, M. Dunlop, and A. Fazakerley (2005), Ion sound wave packets at the quasiperpendicular shock front, *Geophys. Res. Lett.*, **32**, L24106, doi:10.1029/2005GL024660.
- Baumjohann, W., R. A. Treumann, E. Georgescu, G. Haerendel, K.-H. Fornaçon, and U. Auster (1999), Waveform and packet structure of lion roars, *Ann. Geophys.*, **17**, 1528–1534, doi:10.1007/s00585-999-1528-9.
- Bonnell, J. W., F. S. Mozer, G. T. Delory, A. J. Hull, R. E. Ergun, C. M. Cully, V. Angelopoulos, and P. R. Harvey (2008), The Electric Field Instrument (EFI) for THEMIS, *Space Sci. Rev.*, **141**, 303–341, doi:10.1007/s11214-008-9469-2.
- Breneman, A., C. Cattell, K. Kersten, A. Paradise, S. Schreiner, P. J. Kellogg, K. Goetz, and L. B. Wilson III (2013), STEREO and Wind observations of intense cyclotron harmonic waves at the Earth's bow shock and inside the magnetosheath, *J. Geophys. Res. Space Physics*, **118**, 7654–7664, doi:10.1002/2013JA019372.
- Cairns, I. H., and B. F. McMillan (2005), Electron acceleration by lower hybrid waves in magnetic reconnection regions, *Phys. Plasmas*, **12**, 102110, doi:10.1063/1.2080567.
- Cattell, C., et al. (2005), Cluster observations of electron holes in association with magnetotail reconnection and comparison to simulations, *J. Geophys. Res.*, **110**, A01211, doi:10.1029/2004JA010519.
- Comişel, H., M. Scholer, J. Soucek, and S. Matsukiyo (2011), Non-stationarity of the quasi-perpendicular bow shock: Comparison between Cluster observations and simulations, *Ann. Geophys.*, **29**, 263–274, doi:10.5194/angeo-29-263-2011.
- Coroniti, F. V. (1970), Dissipation discontinuities in hydromagnetic shock waves, *J. Plasma Phys.*, **4**, 265–282, doi:10.1017/S0022377800004992.
- Cully, C. M., R. E. Ergun, K. Stevens, A. Nammari, and J. Westfall (2008), The THEMIS digital fields board, *Space Sci. Rev.*, **141**, 343–355, doi:10.1007/s11214-008-9417-1.
- Dimmock, A. P., M. A. Balikhin, V. V. Krasnoselskikh, S. N. Walker, S. D. Bale, and Y. Hobara (2012), A statistical study of the cross-shock electric potential at low Mach number, quasi-perpendicular bow shock crossings using Cluster data, *J. Geophys. Res.*, **117**, A02210, doi:10.1029/2011JA017089.
- Dum, C. T., R. Chodura, and D. Biskamp (1974), Turbulent heating and quenching of the ion sound instability, *Phys. Rev. Lett.*, **32**, 1231–1234, doi:10.1103/PhysRevLett.32.1231.
- Dum, C. T., E. Marsch, and W. Pilipp (1980), Determination of wave growth from measured distribution functions and transport theory, *J. Plasma Phys.*, **23**, 91–113.
- Dyrud, L. P., and M. M. Oppenheim (2006), Electron holes, ion waves, and anomalous resistivity in space plasmas, *J. Geophys. Res.*, **111**, A01302, doi:10.1029/2004JA010482.
- Eastwood, J. P., S. D. Bale, F. S. Mozer, and A. J. Hull (2007), Contributions to the cross shock electric field at a quasiperpendicular collisionless shock, *Geophys. Res. Lett.*, **34**, L17104, doi:10.1029/2007GL030610.
- Edmiston, J. P., and C. F. Kennel (1984), A parametric survey of the first critical Mach number for a fast MHD shock, *J. Plasma Phys.*, **32**, 429–441.
- Ergun, R. E., C. W. Carlson, J. P. McFadden, F. S. Mozer, L. Muschietti, I. Roth, and R. J. Strangeway (1998), Debye-scale plasma structures associated with magnetic-field-aligned electric fields, *Phys. Rev. Lett.*, **81**, 826–829, doi:10.1103/PhysRevLett.81.826.
- Farris, M. H., C. T. Russell, and M. F. Thomsen (1993), Magnetic structure of the low beta, quasi-perpendicular shock, *J. Geophys. Res.*, **98**, 15,285–15,294, doi:10.1029/93JA00958.
- Forslund, D., R. Morse, C. Nielson, and J. Fu (1972), Electron cyclotron drift instability and turbulence, *Phys. Fluids*, **15**, 1303–1318, doi:10.1063/1.1694082.
- Forslund, D. W., R. L. Morse, and C. W. Nielson (1970), Electron cyclotron drift instability, *Phys. Rev. Lett.*, **25**, 1266–1270, doi:10.1103/PhysRevLett.25.1266.
- Franz, J. R., P. M. Kintner, J. S. Pickett, and L.-J. Chen (2005), Properties of small-amplitude electron phase-space holes observed by Polar, *J. Geophys. Res.*, **110**, A09212, doi:10.1029/2005JA011095.
- Fuselier, S. A., and D. A. Gurnett (1984), Short wavelength ion waves upstream of the Earth's bow shock, *J. Geophys. Res.*, **89**, 91–103, doi:10.1029/JA089iA01p00091.
- Gary, S. P. (1981), Microinstabilities upstream of the Earth's bow shock—A brief review, *J. Geophys. Res.*, **86**, 4331–4336, doi:10.1029/JA086iA06p04331.
- Gary, S. P., E. E. Scime, J. L. Phillips, and W. C. Feldman (1994), The whistler heat flux instability: Threshold conditions in the solar wind, *J. Geophys. Res.*, **99**, 23,391–23,399, doi:10.1029/94JA02067.
- Goldman, M. V., D. L. Newman, G. Lapenta, L. Andersson, J. T. Gosling, S. Eriksson, S. Markidis, J. P. Eastwood, and R. Ergun (2014), Čerenkov emission of quasiparallel whistlers by fast electron phase-space holes during magnetic reconnection, *Phys. Rev. Lett.*, **112**(14), 145002, doi:10.1103/PhysRevLett.112.145002.
- Greenstadt, E. W., F. L. Scarf, C. T. Russell, V. Formisano, and M. Neugebauer (1975), Structure of the quasi-perpendicular laminar bow shock, *J. Geophys. Res.*, **80**, 502–514, doi:10.1029/JA080i004p00502.
- Greenstadt, E. W., F. L. Scarf, C. T. Russell, R. E. Holzer, V. Formisano, P. C. Hedgecock, and M. Neugebauer (1977), Structure of a quasi-parallel, quasi-laminar bow shock, *J. Geophys. Res.*, **82**, 651–666, doi:10.1029/JA082i004p00651.
- Gurnett, D. A., F. M. Neubauer, and R. Schwenn (1979a), Plasma wave turbulence associated with an interplanetary shock, *J. Geophys. Res.*, **84**, 541–552, doi:10.1029/JA084iA02p00541.
- Gurnett, D. A., E. Marsch, W. Pilipp, R. Schwenn, and H. Rosenbauer (1979b), Ion acoustic waves and related plasma observations in the solar wind, *J. Geophys. Res.*, **84**, 2029–2038, doi:10.1029/JA084iA05p02029.
- Hellinger, P., P. Trávníček, B. Lembège, and P. Savoini (2007), Emission of nonlinear whistler waves at the front of perpendicular supercritical shocks: Hybrid versus full particle simulations, *Geophys. Res. Lett.*, **34**, L14109, doi:10.1029/2007GL030239.
- Horbury, T. S., et al. (2001), Cluster magnetic field observations of the bowshock: Orientation, motion and structure, *Ann. Geophys.*, **19**, 1399–1409, doi:10.5194/angeo-19-1399-2001.
- Hull, A. J., and J. D. Scudder (2000), Model for the partition of temperature between electrons and ions across collisionless, fast mode shocks, *J. Geophys. Res.*, **105**, 27,323–27,342, doi:10.1029/2000JA900105.
- Hull, A. J., J. D. Scudder, D. E. Larson, and R. Lin (2001), Electron heating and phase space signatures at supercritical, fast mode shocks, *J. Geophys. Res.*, **106**, 15,711–15,734, doi:10.1029/2001JA900001.
- Hull, A. J., D. E. Larson, M. Wilber, J. D. Scudder, F. S. Mozer, C. T. Russell, and S. D. Bale (2006), Large-amplitude electrostatic waves associated with magnetic ramp substructure at Earth's bow shock, *Geophys. Res. Lett.*, **33**, L15104, doi:10.1029/2005GL025564.

- Hull, A. J., L. Muschietti, M. Oka, D. E. Larson, F. S. Mozer, C. C. Chaston, J. W. Bonnell, and G. B. Hospodarsky (2012), Multiscale whistler waves within Earth's perpendicular bow shock, *J. Geophys. Res.*, **117**, A12104, doi:10.1029/2012JA017870.
- Kellogg, P. J., C. A. Cattell, K. Goetz, S. J. Monson, and L. B. Wilson III (2010), Electron trapping and charge transport by large amplitude whistlers, *Geophys. Res. Lett.*, **37**, L20106, doi:10.1029/2010GL044845.
- Kennel, C. F., and H. E. Petschek (1966), Limit on stably trapped particle fluxes, *J. Geophys. Res.*, **71**, 1–28.
- Kennel, C. F., J. P. Edmiston, and T. Hada (1985), A quarter century of collisionless shock research, in *Collisionless Shocks in the Heliosphere: A Tutorial Review*, *Geophys. Monogr. Ser.*, vol. 34, edited by R. G. Stone and B. T. Tsurutani, pp. 1–36, AGU, Washington, D. C., doi:10.1029/GM034p0001.
- Krasnoselskikh, V. V., B. Lembège, P. Savoini, and V. V. Lobzin (2002), Nonstationarity of strong collisionless quasiperpendicular shocks: Theory and full particle numerical simulations, *Phys. Plasmas*, **9**, 1192–1209, doi:10.1063/1.1457465.
- Krauss-Varban, D., and N. Omid (1991), Structure of medium Mach number quasi-parallel shocks: Upstream and downstream waves, *J. Geophys. Res.*, **96**, 17,715–17,731, doi:10.1029/91JA01545.
- Lampe, M., W. M. Manheimer, J. B. McBride, J. H. Orens, K. Papadopoulos, R. Shanny, and R. N. Sudan (1972), Theory and simulation of the beam cyclotron instability, *Phys. Fluids*, **15**, 662–675, doi:10.1063/1.1693961.
- Le Contel, O., et al. (2008), First results of the THEMIS search coil magnetometers, *Space Sci. Rev.*, **141**, 509–534, doi:10.1007/s11214-008-9371-y.
- Lembège, B., and P. Savoini (2002), Formation of reflected electron bursts by the nonstationarity and nonuniformity of a collisionless shock front, *J. Geophys. Res.*, **107**(A3), 1037, doi:10.1029/2001JA900128.
- Lembège, B., P. Savoini, P. Hellinger, and P. M. Trávníček (2009), Nonstationarity of a two-dimensional perpendicular shock: Competing mechanisms, *J. Geophys. Res.*, **114**, A03217, doi:10.1029/2008JA013618.
- Lemons, D. S., and S. P. Gary (1978), Current-driven instabilities in a laminar perpendicular shock, *J. Geophys. Res.*, **83**, 1625–1632, doi:10.1029/JA083iA04p01625.
- Lobzin, V. V., V. V. Krasnoselskikh, J. Bosqued, J. Pinçon, S. J. Schwartz, and M. Dunlop (2007), Nonstationarity and reformation of high-Mach-number quasiperpendicular shocks: Cluster observations, *Geophys. Res. Lett.*, **34**, L05107, doi:10.1029/2006GL029095.
- Lu, Q. M., B. Lembège, J. B. Tao, and S. Wang (2008), Perpendicular electric field in two-dimensional electron phase-holes: A parameter study, *J. Geophys. Res.*, **113**, A11219, doi:10.1029/2008JA013693.
- Malaspina, D. M., D. L. Newman, L. B. Wilson III, K. Goetz, P. J. Kellogg, and K. Kersten (2013), Electrostatic solitary waves in the solar wind: Evidence for instability at solar wind current sheets, *J. Geophys. Res. Space Physics*, **118**, 591–599, doi:10.1002/jgra.50102.
- Matsukiyo, S., and M. Scholer (2006), On microinstabilities in the foot of high Mach number perpendicular shocks, *J. Geophys. Res.*, **111**, A06104, doi:10.1029/2005JA011409.
- McFadden, J. P., C. W. Carlson, D. Larson, M. Ludlam, R. Abiad, B. Elliott, P. Turin, M. Marckwordt, and V. Angelopoulos (2008a), The THEMIS ESA plasma instrument and in-flight calibration, *Space Sci. Rev.*, **141**, 277–302, doi:10.1007/s11214-008-9440-2.
- McFadden, J. P., C. W. Carlson, D. Larson, J. Bonnell, F. Mozer, V. Angelopoulos, K.-H. Glassmeier, and U. Auster (2008b), THEMIS ESA first science results and performance issues, *Space Sci. Rev.*, **141**, 477–508, doi:10.1007/s11214-008-9433-1.
- Mellott, M. M., and E. W. Greenstadt (1988), Plasma waves in the range of the lower hybrid frequency—ISEE 1 and 2 observations at the Earth's bow shock, *J. Geophys. Res.*, **93**, 9695–9708, doi:10.1029/JA093iA09p09695.
- Mitchell, J. J., and S. J. Schwartz (2014), Isothermal magnetosheath electrons due to nonlocal electron cross talk, *J. Geophys. Res. Space Physics*, **119**, 1080–1093, doi:10.1002/2013JA019211.
- Mitchell, J. J., S. J. Schwartz, and U. Auster (2012), Electron cross talk and asymmetric electron distributions near the Earth's bowshock, *Ann. Geophys.*, **30**, 503–513, doi:10.5194/angeo-30-503-2012.
- Moreira, A. (1983), Stability analysis of magnetosheath ion roars, *Planet. Space Sci.*, **31**, 1165–1170, doi:10.1016/0032-0633(83)90105-8.
- Mozer, F. S., and D. Sundkvist (2013), Electron demagnetization and heating in quasi-perpendicular shocks, *J. Geophys. Res. Space Physics*, **118**, 5415–5420, doi:10.1002/jgra.50534.
- Muschietti, L., and B. Lembège (2013), Microturbulence in the electron cyclotron frequency range at perpendicular supercritical shocks, *J. Geophys. Res. Space Physics*, **118**, 2267–2285, doi:10.1002/jgra.50224.
- Omura, Y., H. Matsumoto, T. Miyake, and H. Kojima (1996), Electron beam instabilities as generation mechanism of electrostatic solitary waves in the magnetotail, *J. Geophys. Res.*, **101**, 2685–2698, doi:10.1029/95JA03145.
- Paschmann, G., N. Sckopke, I. Papamastorakis, J. R. Asbridge, S. J. Bame, and J. T. Gosling (1981), Characteristics of reflected and diffuse ions upstream from the Earth's bow shock, *J. Geophys. Res.*, **86**, 4355–4364, doi:10.1029/JA086iA06p04355.
- Petkaki, P., and M. P. Freeman (2008), Nonlinear dependence of anomalous ion-acoustic resistivity on electron drift velocity, *Astrophys. J.*, **686**, 686–693, doi:10.1086/590654.
- Petkaki, P., M. P. Freeman, T. Kirk, C. E. J. Watt, and R. B. Horne (2006), Anomalous resistivity and the nonlinear evolution of the ion-acoustic instability, *J. Geophys. Res.*, **111**, A01205, doi:10.1029/2004JA010793.
- Petschek, H. E. (1958), Aerodynamic dissipation, *Rev. Mod. Phys.*, **30**, 966–974, doi:10.1103/RevModPhys.30.966.
- Riquelme, M. A., and A. Spitkovsky (2011), Electron injection by whistler waves in non-relativistic shocks, *Astrophys. J.*, **733**, 63, doi:10.1088/0004-637X/733/1/63.
- Roux, A., O. Le Contel, C. Coillot, A. Bouabdellah, B. de La Porte, D. Alison, S. Ruocco, and M. C. Vassal (2008), The search coil magnetometer for THEMIS, *Space Sci. Rev.*, **141**, 265–275, doi:10.1007/s11214-008-9455-8.
- Sagdeev, R. Z. (1966), Cooperative phenomena and shock waves in collisionless plasmas, *Rev. Plasma Phys.*, **4**, 23.
- Scholer, M., H. Kucharek, and I. Shinohara (2003), Short large-amplitude magnetic structures and whistler wave precursors in a full-particle quasi-parallel shock simulation, *J. Geophys. Res.*, **108**(A7), 1273, doi:10.1029/2002JA009820.
- Schwartz, S. J., and D. Burgess (1991), Quasi-parallel shocks—A patchwork of three-dimensional structures, *Geophys. Res. Lett.*, **18**, 373–376, doi:10.1029/91GL00138.
- Scudder, J. D., T. L. Aggson, A. Mangeney, C. Lacombe, and C. C. Harvey (1986), The resolved layer of a collisionless, high beta, supercritical, quasi-perpendicular shock wave: 1. Rankine-Hugoniot geometry, currents, and stationarity, *J. Geophys. Res.*, **91**, 11,019–11,052, doi:10.1029/JA091iA10p11019.
- Sentman, D. D., M. M. Hoppe, M. F. Thomsen, S. P. Gary, and W. C. Feldman (1983), The oblique whistler instability in the Earth's foreshock, *J. Geophys. Res.*, **88**, 2048–2056, doi:10.1029/JA088iA03p02048.
- Silin, I., J. Büchner, and A. Vaivads (2005), Anomalous resistivity due to nonlinear lower-hybrid drift waves, *Phys. Plasmas*, **12**(6), 062902, doi:10.1063/1.1927096.
- Singh, N., S. M. Loo, B. E. Wells, and C. Deverapalli (2000), Three-dimensional structure of electron holes driven by an electron beam, *Geophys. Res. Lett.*, **27**, 2469–2472, doi:10.1029/2000GL003766.

- Singh, N., S. M. Loo, and B. E. Wells (2001), Electron hole as an antenna radiating plasma waves, *Geophys. Res. Lett.*, **28**, 1371–1374, doi:10.1029/2000GL012652.
- Su, Y., Q. Lu, X. Gao, C. Huang, and S. Wang (2012), Ion dynamics at supercritical quasi-parallel shocks: Hybrid simulations, *Phys. Plasmas*, **19**(9), 092108, doi:10.1063/1.4752219.
- Sundkvist, D., V. Krasnoselskikh, S. D. Bale, S. J. Schwartz, J. Soucek, and F. Mozer (2012), Dispersive nature of high Mach Number collisionless plasma shocks: Poynting flux of oblique whistler waves, *Phys. Rev. Lett.*, **108**, 025002, doi:10.1103/PhysRevLett.108.025002.
- Tidman, D. A., and N. A. Krall (1971), *Shock Waves in Collisionless Plasmas*, John Wiley, New York.
- Tidman, D. A., and T. G. Northrop (1968), Emission of plasma waves by the Earth's bow shock, *J. Geophys. Res.*, **73**, 1543–1553, doi:10.1029/JA073i005p01543.
- Torrence, C., and G. P. Compo (1998), Wavelet analysis software, atmospheric and oceanic sciences, Univ. of Colorado, Boulder, Colo. [Available at <http://paos.colorado.edu/research/wavelets/>.]
- Treumann, R. A. (2009), Fundamentals of collisionless shocks for astrophysical application: 1. Non-relativistic shocks, *Astron. Astrophys. Rev.*, **17**, 409–535, doi:10.1007/s00159-009-0024-2.
- Tsubouchi, K., and B. Lembège (2004), Full particle simulations of short large-amplitude magnetic structures (SLAMS) in quasi-parallel shocks, *J. Geophys. Res.*, **109**, A02114, doi:10.1029/2003JA010014.
- Umeda, T., Y. Omura, T. Miyake, H. Matsumoto, and M. Ashour-Abdalla (2006), Nonlinear evolution of the electron two-stream instability: Two-dimensional particle simulations, *J. Geophys. Res.*, **111**, A10206, doi:10.1029/2006JA011762.
- Umeda, T., Y. Kidani, S. Matsukiyo, and R. Yamazaki (2012), Microinstabilities at perpendicular collisionless shocks: A comparison of full particle simulations with different ion to electron mass ratio, *Phys. Plasmas*, **19**(4), 042109, doi:10.1063/1.3703319.
- Vedenov, A. A. (1963), Quasi-linear plasma theory (theory of a weakly turbulent plasma), *J. Nucl. Energy*, **5**, 169–186, doi:10.1088/0368-3281/5/3/305.
- Walker, S. N., M. A. Balikhin, H. S. C. K. Alleyne, Y. Hobara, M. André, and M. W. Dunlop (2008), Lower hybrid waves at the shock front: A reassessment, *Ann. Geophys.*, **26**, 699–707.
- Wilson, L. B., III (2010), The microphysics of collisionless shocks, PhD thesis, Univ. of Minnesota, Minneapolis, Minn. [Available at <http://lynn.b.wilsoniii@gmail.com>.]
- Wilson, L. B., III, C. Cattell, P. J. Kellogg, K. Goetz, K. Kersten, L. Hanson, R. MacGregor, and J. C. Kasper (2007), Waves in interplanetary shocks: A wind/WAVES study, *Phys. Rev. Lett.*, **99**(4), 041101, doi:10.1103/PhysRevLett.99.041101.
- Wilson, L. B., III, C. A. Cattell, P. J. Kellogg, K. Goetz, K. Kersten, J. C. Kasper, A. Szabo, and K. Meziane (2009), Low-frequency whistler waves and shocklets observed at quasi-perpendicular interplanetary shocks, *J. Geophys. Res.*, **114**, A10106, doi:10.1029/2009JA014376.
- Wilson, L. B., III, C. A. Cattell, P. J. Kellogg, K. Goetz, K. Kersten, J. C. Kasper, A. Szabo, and M. Wilber (2010), Large-amplitude electrostatic waves observed at a supercritical interplanetary shock, *J. Geophys. Res.*, **115**, A12104, doi:10.1029/2010JA015332.
- Wilson, L. B., III, C. A. Cattell, P. J. Kellogg, J. R. Wygant, K. Goetz, A. Breneman, and K. Kersten (2011), The properties of large amplitude whistler mode waves in the magnetosphere: Propagation and relationship with geomagnetic activity, *Geophys. Res. Lett.*, **38**, L17107, doi:10.1029/2011GL048671.
- Wilson, L. B., III et al. (2012), Observations of electromagnetic whistler precursors at supercritical interplanetary shocks, *Geophys. Res. Lett.*, **39**, L08109, doi:10.1029/2012GL051581.
- Wilson, L. B., III et al. (2013a), Electromagnetic waves and electron anisotropies downstream of supercritical interplanetary shocks, *J. Geophys. Res. Space Physics*, **118**, 5–16, doi:10.1029/2012JA018167.
- Wilson, L. B., III et al. (2013b), Shocklets, SLAMS, and field-aligned ion beams in the terrestrial foreshock, *J. Geophys. Res. Space Physics*, **118**, 957–966, doi:10.1029/2012JA018186.
- Wilson, L. B., III, D. G. Sibeck, A. W. Breneman, O. Le Contel, C. Cully, D. L. Turner, V. Angelopoulos, and D. M. Malaspina (2014), Quantified energy dissipation rates in the terrestrial bow shock: 1. Analysis techniques and methodology, *J. Geophys. Res. Space Physics*, doi:10.1002/2014JA019929.
- Wu, C. S., D. Winske, K. Papadopoulos, Y. M. Zhou, S. T. Tsai, and S. C. Guo (1983), A kinetic cross-field streaming instability, *Phys. Fluids*, **26**, 1259–1267, doi:10.1063/1.864285.
- Wu, C. S., et al. (1984), Microinstabilities associated with a high Mach number, perpendicular bow shock, *Space Sci. Rev.*, **37**, 63–109, doi:10.1007/BF00213958.
- Wygant, J. R., M. Bensadoun, and F. S. Mozer (1987), Electric field measurements at subcritical, oblique bow shock crossings, *J. Geophys. Res.*, **92**, 11,109–11,121, doi:10.1029/JA092iA10p11109.
- Wygant, J. R., et al. (2000), Polar spacecraft based comparisons of intense electric fields and Poynting flux near and within the plasma sheet-tail lobe boundary to UVI images: An energy source for the aurora, *J. Geophys. Res.*, **105**, 18,675–18,692, doi:10.1029/1999JA900500.
- Yang, Z. W., Q. M. Lu, B. Lembège, and S. Wang (2009), Shock front nonstationarity and ion acceleration in supercritical perpendicular shocks, *J. Geophys. Res.*, **114**, A03111, doi:10.1029/2008JA013785.
- Yoon, P. H., and A. T. Y. Lui (2006), Quasi-linear theory of anomalous resistivity, *J. Geophys. Res.*, **111**, A02203, doi:10.1029/2005JA011482.
- Yoon, P. H., and A. T. Y. Lui (2007), Anomalous resistivity by fluctuation in the lower-hybrid frequency range, *J. Geophys. Res.*, **112**, A06207, doi:10.1029/2006JA012209.